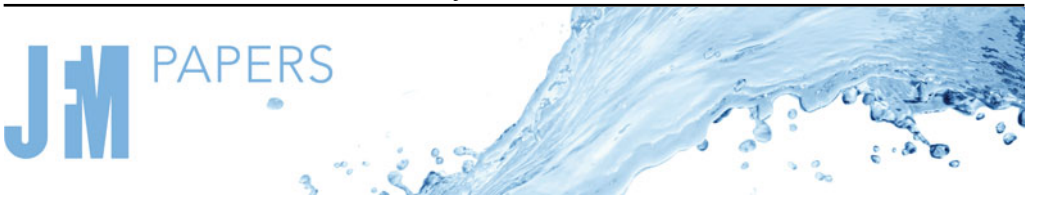
J. Fluid Mech. (2026), *vol.* 1031, A2, doi:10.1017/jfm.2026.11260



Surfactant effects on gravity-capillary waves

Rui Yang[1], **Zehua Liu**[1], **Palas Kumar Farsoiya**[2], **Stéphane Popinet**[3] and **Luc Deike**[1,4]

[1]Department of Mechanical and Aerospace Engineering, Princeton University, Princeton, NJ 08540, USA

[2]Department of Chemical Engineering, Indian Institute of Technology Roorkee, Roorkee, Uttarakhand 247667, India

[3]Sorbonne Université, CNRS, Institut Jean Le Rond d'Alembert, F-75005 Paris, France

[4]High Meadows Environmental Institute, Princeton University, Princeton, NJ 08540, USA

Corresponding authors: Rui Yang, ruiyang@princeton.edu; Luc Deike, ldeike@princeton.edu

(Received 15 August 2025; revised 4 December 2025; accepted 28 January 2026)

Surfactants at the air–sea interface are known to alter surface wave dynamics by modifying surface tension and Marangoni stresses. In this study, we perform two-dimensional direct numerical simulations of gravity-capillary waves with insoluble surfactants using a coupled phase field and volume-of-fluid method. We consider a nonlinear equation of state for surface tension and resolve Marangoni stresses induced by surfactant concentration gradients. We explore a broad parameter space characterised by initial wave steepness ak, Bond number Bo (comparing gravity and surface tension), Reynolds number Re (comparing inertia and viscosity), and the importance of surfactant concentration and strength of the gradient, characterised by a surfactant parameter β. We analyse the impact of surfactants on wave patterns, surface roughness, wave breaking, energy dissipation and surface vorticity. Our results reveal a non-monotonic dependence of wave shape, roughness, vorticity and energy dissipation on β, which is found to be governed by Marangoni effects that peak at intermediate surfactant concentrations. Wave regime transition at high Bo is governed by an effective Bo, which accounts for the reduction in surface tension induced by surfactants. We further introduce a rescaled parameter $Bo\,Re^{-1/2}\,(ak)^{-1}$ based on force balance, which collapses the transition boundaries across different Re. These findings provide a systematic understanding of surfactant-modulated wave dynamics for both laboratory and geophysical applications.

Key words: air/sea interactions, multiphase flow, wave breaking

© The Author(s), 2026. Published by Cambridge University Press. This is an Open Access article, distributed under the terms of the Creative Commons Attribution licence (https://creativecommons.org/licenses/by/4.0/), which permits unrestricted re-use, distribution and reproduction, provided the original article is properly cited.

https://doi.org/10.1017/jfm.2026.11260 Published online by Cambridge University Press

1. Introduction

1.1. *The broader context*

Surface-active molecules and/or particles, commonly known as surfactants, play a significant role in modulating physical processes near the air–sea interface. They alter interfacial properties by reducing surface tension and introducing surface elasticity and viscosity (Wurl *et al.* 2011; Manikantan & Squires 2020) across scales, from bubble rise and bursting to wave breaking (Deike 2022). Such changes have been shown to suppress short gravity-capillary waves (Alpers & Hühnerfuss 1989), affect air–sea gas exchange rates (Bell *et al.* 2015), modify the bubble dynamics, including their lifetimes, coalescence and bursting (Poulain, Villermaux & Bourouiba 2018; Néel & Deike 2021; Shaw & Deike 2021), and potentially influence wave–structure interaction dynamics (Luo *et al.* 2024; Magdalena *et al.* 2025; Xu *et al.* 2025). Ocean surfaces are covered by a heterogeneous microlayer composed of multiple surfactant species (lipids, polysaccharides and proteins, chromophoric dissolved organic matter) (Wurl *et al.* 2011; Burrows *et al.* 2014; King *et al.* 2019), whose compositions vary in time and space due to biological activity, wind–wave forcing, and bubble bursting. This multicomponent nature implies complex interfacial properties, and quantitative characterisation remains unclear, in part because of the lack of knowledge of a governing equation of state (EOS) linking surface tension and surfactant concentration that varies across surfactant species.

Surfactants influence not only the interface but also the behaviour of droplets and bubbles near the ocean surface and the atmosphere–ocean gas flux (Tsai & Liu 2003; Bell *et al.* 2015). In the subsurface region, surfactant-laden interfaces slow down bubble rise velocities by suppressing interfacial mobility (Takagi & Matsumoto 2011), while at the surface, they affect bubble coalescence, surface residence time, and the size distribution of droplets ejected from bursting bubbles (Néel & Deike 2021; Néel *et al.* 2022). These phenomena have implications for aerosol production, air–sea exchange, and remote sensing of the ocean surface.

The impact of surfactants on wave breaking has been investigated through both experimental and numerical studies. Liu & Duncan (2003, 2006, 2007) conducted a series of laboratory experiments on gentle spilling breakers, and found that the presence of surfactants can alter the wave breaking process. Specifically, surfactants were shown to reshape the wave crest and suppress the formation of parasitic capillary waves at the onset of breaking. At sufficiently high concentrations, they observed the emergence of small plunging jets and the entrapment of air pockets on the front face of the wave. More recently, Erinin *et al.* (2023) carried out detailed experiments on plunging breakers with insoluble surfactants, and quantified how varying surfactant concentrations affect crest shape, surface roughness and energy dissipation. Xu & Perlin (2023) conducted experiments in a convergent channel, and demonstrated that surfactants not only suppress parasitic capillary waves, but also effectively increase the local Bond number, thereby promoting wave breaking in small-scale, capillary-gravity wave regimes.

The change in wave behaviour described by Erinin *et al.* (2023) was related to how surfactant surface concentration Γ affects the surface tension of the interface via some EOS $\gamma = \gamma(\Gamma)$ (often referred to as the surface tension isotherm) (Manikantan & Squires 2020). Erinin *et al.* (2023) had performed measurements of the surface tension isotherm using a Langmuir trough, and discussed the wave pattern in terms of the estimated surface tension gradient leading to the Marangoni stress.

The experimental studies provide a physical picture of coupled interfacial phenomena with Marangoni effects across scales, from bubbles and drops (Pierre, Poujol & Séon

https://doi.org/10.1017/jfm.2026.11260 Published online by Cambridge University Press

2022; Wang *et al.* 2026) to waves (Erinin *et al.* 2023; Xu & Perlin 2023), while interfacial fluid mechanics problems with surfactants are also dependent on initial conditions that are sometimes difficult to control in experiments. Numerical simulations can provide a comprehensive picture of surfactant transport and distribution, and their effect on hydrodynamics, as a result of the ability to control initial conditions and determine all flow field data. Advances in numerical modelling (Liao, Franses & Basaran 2006; Constante-Amores *et al.* 2021; Pico *et al.* 2024; Wang *et al.* 2025) have enabled the simulation of surfactant-laden flows using a variety of approaches, such as the boundary-element method (Yon & Pozrikidis 1998), front-tracking method (Muradoglu & Tryggvason 2014), diffuse-interface method (Jain 2024), hybrid approaches coupling level-set and volume-of-fluid (VOF) (Saini *et al.* 2025), and so on. Numerical simulations based on hybrid approaches coupling level-set and front-tracking by Ceniceros (2003) demonstrated that surfactants modify wave evolution by accumulating in regions of compression, leading to strong surface tension gradients that generate Marangoni flows opposing the surface motion. These effects are particularly relevant for both spilling and plunging breaker regimes. Simulations based on geometric VOF coupled with phase field by Farsoiya *et al.* (2024) for insoluble surfactants showed that the bubble rising velocity in a quiescent liquid decreases and reaches a limiting value at high Marangoni numbers. These efforts provide new insight into the coupling between interfacial surfactant dynamics and free-surface flow behaviour. Eshima *et al.* (2025) combine such numerical frameworks with experiments and measurements of the EOS for surface tension to quantify the role of insoluble surfactant on jet drop formation by bubble bursting.

1.2. *Gravity-capillary waves in the presence of insoluble surfactants: non-dimensional numbers*

The gravity-capillary wave problem in deep water without surfactant can be defined by a set of dimensionless parameters (Iafrati 2011; Deike *et al.* 2015, 2016; Mostert, Popinet & Deike 2022). The wavelength λ sets the characteristic horizontal length scale of the wave, and the wave amplitude a controls the initial strength of the nonlinearities, while the restoring forces are the gravitational acceleration g and the (static) surface tension σ_c in clean conditions. The air and water are characterised by their density and viscosity. Without surfactant, the system is then characterised by five non-dimensional parameters (Deike, Popinet & Melville 2015):

$$ak, \quad Bo = \frac{\Delta\rho\, g}{\sigma_c k^2}, \quad Re = \frac{\sqrt{g\lambda^3}}{\nu_w}, \quad \frac{\rho_a}{\rho_w}, \quad \frac{\mu_a}{\mu_w}, \tag{1.1}$$

where ak is the wave steepness, $k = 2\pi/\lambda$ is the wavenumber, Bo is the Bond number comparing gravitational to capillary forces, and Re is the Reynolds number based on the gravity wave phase speed $c_0 = \sqrt{g/k}$ and wavelength λ, and the density and viscosity ratios. The subscript a represents the properties in the air phase, and the subscript w represents the properties in the water phase.

We consider here surfactants at the water surface assumed to be insoluble and characterised by their concentration $\Gamma(l)$ along the surface arc length l as they get advected and compressed by the wave motion. The concentration gradients along the surface $\partial\Gamma/\partial l$ will introduce gradients in surface tension forces, or Marangoni stresses $\partial\sigma/\partial l$ related to the concentration gradients through the surfactant EOS.

https://doi.org/10.1017/jfm.2026.11260 Published online by Cambridge University Press

The relative strength of the Marangoni forcing can be quantified locally by comparison with the viscous stress, and we define a local Marangoni number

$$Ma_{loc} = \frac{E_0}{\mu_w c_0} = \frac{\partial\sigma}{\partial l}\frac{\lambda}{\sigma_c}(2\pi)^{3/2}\frac{Re}{Bo}, \tag{1.2}$$

where $E_0 = \lambda\,\partial\sigma/\partial l$ represents the local surface tension gradient (or Marangoni modulus) (Manikantan & Squires 2020; Erinin *et al.* 2023). While this quantity is usually not accessible experimentally, numerical simulations allow for explicit tracking of surface surfactant transport and the Marangoni stress (Farsoiya *et al.* 2024; Eshima *et al.* 2025). Here, Ma_{loc} characterises the ratio of interfacial elasticity or Marangoni stress to viscous stress to get the detailed local Marangoni forcing.

We also see that Ma_{loc} is inversely proportional to Bo (through the static surface tension dependence), indicating that Marangoni effects become more significant in low-Bo regimes, while also depending on the Reynolds number. Since the strength of the surface tension gradients will depend on the strength of the surfactant accumulation/compression along the interface, the initial wave slope is also expected to be important.

To characterise the advective surfactant transport at the interface, the Péclet number is introduced:

$$Pe = c_0\lambda/D_s, \tag{1.3}$$

where D_s is the interfacial surfactant diffusivity, and the absorption/desorption from the bulk is neglected. In our study, the interfacial surfactant transport is dominated by advection, and the interfacial diffusion is negligible.

Contamination of gravity-capillary waves has long been assumed to smooth the surface (Franklin & Brownrigg 1774; Mertens 2006), with an influence on the sea surface roughness and implications for radar and optical remote sensing applications (Erinin *et al.* 2023; Lohse 2023; Davis *et al.* 2025). The classic metric for surface roughness is the mean square slope s^2, which is defined as

$$s^2 = \langle(\nabla\eta)^2\rangle, \tag{1.4}$$

where $\langle\cdot\rangle$ is the spatial averaging operator, and η is the surface height. As we will see, the mean square slope will be tightly related to the strength of Marangoni flows for gravity-capillary waves.

1.3. *Outline*

In this study, we perform two-dimensional direct numerical simulations of surface waves with insoluble surfactants using a coupled phase field and VOF framework, following the implementation of Farsoiya *et al.* (2024) and Saini *et al.* (2025). Our formulation incorporates a nonlinear EOS for surface tension with surfactant, informed by experimental observations, and accounts for the Marangoni effects induced by surfactant concentration gradients. We investigate how surfactant concentration influences the formation and suppression of parasitic capillary waves, the transition to wave breaking, and the associated energy dissipation across a broad range of non-dimensional control parameters. In addition to presenting detailed numerical results, we provide a physical understanding of the non-monotonic dependence of wave roughness and energy dissipation on the surfactant, and show that it originates from Marangoni stresses that peak at intermediate concentrations. We also develop a physically based predictive framework that unifies the phase space throughout different control parameters, and quantifies the influence of surfactants on surface wave dynamics.

https://doi.org/10.1017/jfm.2026.11260 Published online by Cambridge University Press

The paper is organised as follows. Section 2 presents the numerical model and governing equations, including the EOS, dimensionless control parameters and response parameters. Section 3 analyses how surfactants influence wave shape and roughness, revealing a non-monotonic response to Marangoni forcing. Section 4 further quantifies the surfactant effect with a phase diagram, and physically explains the underlying mechanisms through scaling analysis and force balance. Section 5 shows the effect of surfactants on the total energy dissipation and surface vorticity. Finally, § 6 summarises the main findings and outlines implications for ocean wave modelling.

2. Numerical methods

2.1. *Governing equations*

We solve the two-dimensional, incompressible, two-phase Navier–Stokes equations with interfacial effects, including Marangoni stresses from surface tension gradients. The interface between water and air is reconstructed by a coupled level-set/VOF method. The equations can be written as

$$\boldsymbol{\nabla}\cdot\boldsymbol{u}=0, \tag{2.1}$$

$$\rho\left(\frac{\partial \boldsymbol{u}}{\partial t}+\boldsymbol{u}\cdot\boldsymbol{\nabla}\boldsymbol{u}\right)=-\boldsymbol{\nabla}p+\boldsymbol{\nabla}\cdot(\mu(\boldsymbol{\nabla}\boldsymbol{u}+\boldsymbol{\nabla}\boldsymbol{u}^{\mathrm{T}}))+\delta_s\sigma\kappa\boldsymbol{n}+\delta_s\,\boldsymbol{\nabla}_s\sigma, \tag{2.2}$$

where $\boldsymbol{u}$ is the fluid velocity, ρ is the fluid density, p is the pressure, μ is the dynamic viscosity, σ is the surface tension, and κ is the interface curvature. The unit normal vector to the interface is denoted by $\boldsymbol{n}$. The function δ_s is a Dirac delta function that localises the surface tension term at the interface, and $\boldsymbol{\nabla}_s=(\boldsymbol{I}-\boldsymbol{nn})\cdot\boldsymbol{\nabla}$ is the surface gradient operator (Stone 1990; Farsoiya *et al.* 2024). The last term represents the tangential Marangoni stress due to gradients in σ along the interface.

The Marangoni force is computed using an integral formulation for surface tension (Abu-Al-Saud, Popinet & Tchelepi 2018), and surfactant transport is modelled using a coupled phase-field/VOF method developed by Jain (2024) and implemented in Farsoiya *et al.* (2024). The evolution of the insoluble surfactant concentration is given by

$$\frac{\partial c}{\partial t}+\boldsymbol{\nabla}\cdot(\boldsymbol{u}c)=\boldsymbol{\nabla}\cdot\left[D_s\left\{\boldsymbol{\nabla}c-\frac{2(0.5-\phi)\boldsymbol{n}c}{\varepsilon}\right\}\right], \tag{2.3}$$

where $c=\Gamma\phi(1-\phi)/\varepsilon$ is the volumetric surfactant concentration, and Γ is the local surface surfactant concentration used to calculate σ through the EOS. The second term on the right-hand side is an anti-diffusion term that keeps the scalar c concentrated at the interface, which ensures that surfactant remains restricted to the interface, thereby numerically enforcing the insolubility condition. Here, ε is the phase field interface thickness, which is set to $0.75\,\Delta x_{min}$, where Δx_{min} is the minimum grid spacing, following Farsoiya *et al.* (2024). Sensitivity tests on the values of ε have been performed, and the chosen value $\varepsilon=0.75\,\Delta x_{min}$ provides a good balance between accuracy and numerical stability. More details are given in Appendix A. The scalar field ϕ defines the interface location and is governed by a conservative phase field equation

$$\frac{\partial \phi}{\partial t}+\boldsymbol{\nabla}\cdot(\boldsymbol{u}\phi)=\boldsymbol{\nabla}\cdot\left\{\zeta\left\{\varepsilon\,\boldsymbol{\nabla}\phi-\frac{1}{4}\left[1-\tanh^2\left(\frac{\psi}{2\varepsilon}\right)\right]\frac{\boldsymbol{\nabla}\psi}{|\boldsymbol{\nabla}\psi|}\right\}\right\}, \tag{2.4}$$

where ζ is a velocity scale parameter set to $\zeta=1.1\,|\boldsymbol{u}|_{max}$, and $\psi=\varepsilon\log[(\phi+\delta)/(1-\phi+\delta)]$ is an auxiliary signed-distance-like function with a small regularisation parameter

https://doi.org/10.1017/jfm.2026.11260 Published online by Cambridge University Press

$\delta = 10^{-6}$, following Farsoiya *et al.* (2024). Sensitivity tests to the values of ζ are performed in Appendix A, which show negligible effects on the results. Therefore, the surfactant is introduced by coupling (2.3) and (2.4) to solve for Γ and then contribute to σ by the EOS, which specific formulation is given in the next subsection. By introducing a phase field model, we avoid the explicit tracking of surfactant transport on a sharp interface with large deformations, which improves the solver's numerical stability. The trade-off comes at the cost of an increased computational complexity and the introduction of additional numerical parameters for the phase field equation, which we test in Appendix A. Note that as verified in Farsoiya *et al.* (2024), the present numerical scheme has good surfactant mass conservation properties. This was also verified in the present configuration, with errors below 4 %.

This coupled framework is implemented in the open-source solver Basilisk (https://basilisk.fr) (Popinet 2009, 2018), which supports adaptive mesh refinement and parallel scalability, and has been extensively applied to multiphase flow problems. The spatial discretisation uses a quadtree (in two dimensions), where each computational cell can be subdivided into four child cells. The base of the tree, known as the root cell, is assigned level zero, and each refinement step increases the level by one. The maximum refinement level, denoted by L, determines the finest resolution available in the simulation. Accurate simulation of surface waves requires high spatial resolution near the interface and in the boundary layers, where vorticity develops and energy dissipation mainly occurs. The wavelet adaptive refinement criteria are based on the volume fraction field, velocity field, phase field and concentration field, with corresponding thresholds $\epsilon_f = 10^{-3}$, $\epsilon_u = 5 \times 10^{-3}$, $\epsilon_\phi = 10^{-3}$, $\epsilon_c = 10^{-3}$, ensuring that the key physical processes are well resolved.

2.2. *The EOS*

The EOS is typically nonlinear with surfactant concentration, and different types of surfactants can lead to different EOS (Liao *et al.* 2006; Muradoglu & Tryggvason 2008). For surface waves, with the assumption of insolubility, a relationship between surface tension and surfactant concentration was experimentally measured in the case of insoluble surfactant Triton X using a Langmuir trough (Erinin *et al.* 2023). The measured relationship presents some key features: it shows that surface tension decreases nonlinearly with increasing surfactant concentration, and approaches a saturation limit corresponding to the maximum surface packing density. Therefore, we consider a smooth EOS with a two-parameter tanh model (Liao *et al.* 2006; Farsoiya *et al.* 2024; Eshima *et al.* 2025):

$$\frac{\sigma}{\sigma_c} = 1 - \Delta\sigma_\infty \tanh\left(\frac{\beta}{\Delta\sigma_\infty}\frac{\Gamma}{\Gamma_0}\right), \tag{2.5}$$

where σ_c is the surface tension of a clean (surfactant-free) interface, Γ is the local surfactant concentration, and Γ_0 is the initial (uniform) surfactant concentration. This EOS originates from Henry's isotherm, which describes a linear dependence of surface tension on surfactant concentration (Manikantan & Squires 2020). The use of a hyperbolic tangent function provides a smooth transition of surface tension at different surfactant concentrations. This form recovers the linear relation at low concentrations while smoothly approaching a finite minimum value at high concentrations, so as to avoid artificial cut-offs or discontinuities that could cause numerical instability. This EOS also captures the basic nonlinear trend observed in experiments (Erinin *et al.* 2023) while remaining mathematically simple and computationally efficient. Although it is not a one-to-one comparison, and the specific choice of parameters (β, Δ) modifies the magnitude of the

https://doi.org/10.1017/jfm.2026.11260 Published online by Cambridge University Press

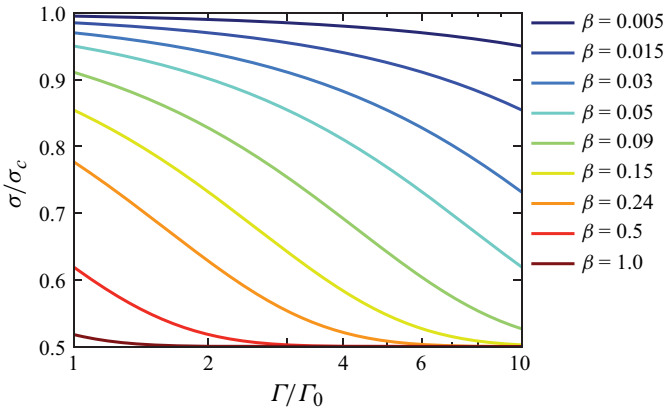


Figure 1. Illustration of the nonlinear EOS used in this study: Normalised surface tension σ/σ_c as a function of Γ/Γ_0 for increasing values of the surfactant parameter β (representing surfactant strength and concentration) with $\Delta\sigma_\infty = 0.5$.

Marangoni number, the underlying physics governed by surface tension gradients should remain consistent.

We would also like to point out that there is no obvious good choice in terms of EOS for insoluble surfactant in terms of experimental measurements in the context of surfactant effects on surface waves. Most experimental studies do not report the EOS, or do not measure it. Part of the puzzle is to find out how much the specific surfactant, or mixture of surfactant, will affect the physics of surface waves. Detailed comparison between experiments and simulations would require knowledge of the measured EOS. These questions have motivated our choice of a simple EOS with a small number of parameters. We also used this EOS in a separate paper on jet drops formed by bubble bursting, demonstrating close agreement to experiments where we had measured the Langmuir isotherm as a way to access the EOS (Eshima *et al.* 2025).

Two additional dimensionless parameters are therefore introduced as we consider insoluble surfactant, β and $\Delta\sigma_\infty$, which is physically related to the surfactant concentration and strength, and controls the slope of $\sigma(\beta)$ and the maximum reduction in surface tension, respectively. This formulation ensures that $\sigma \to \sigma_c(1 - \Delta\sigma_\infty)$ as $\Gamma \gg \Gamma_0$, and recovers the linear behaviour for $\Gamma \ll \Gamma_0$, i.e. $\sigma \approx \sigma_c(1 - \beta\Gamma/\Gamma_0)$ (Farsoiya *et al.* 2024). The parameter β is tightly linked to the Marangoni number. During the surfactant redistribution process, the total interfacial surfactant mass is conserved. Adsorption and desorption processes are neglected in the present model.

Figure 1 presents σ/σ_c as a function of Γ/Γ_0 from (2.5) for different β with fixed $\Delta\sigma_\infty = 0.5$. This shows how the sensitivity of surface tension to surface compression evolves with increasing β. For small values of β, as Γ/Γ_0 increases from 1, the normalised surface tension σ/σ_c initially decreases slowly, followed by an approximately linear decrease with Γ/Γ_0. For larger β, σ/σ_c decreases continuously as Γ/Γ_0 increases, with the slope of $\sigma(\Gamma)$ also decreasing. Parameter β influences not only the slope but also the initial surface tension at uniform concentration ($\Gamma/\Gamma_0 = 1$), which decreases with increasing β. We note again that the fact that β controls $\mathrm{d}\sigma/\mathrm{d}l$ and the initial surface tension is a feature common to any nonlinear EOS.

In the following, the value of the surfactant parameter $\Delta\sigma_\infty$ is fixed at 0.5, which gives a $\sigma(\Gamma)$ EOS similar to those measured experimentally by Erinin *et al.* (2023) for

https://doi.org/10.1017/jfm.2026.11260 Published online by Cambridge University Press

Triton-X using a Langmuir trough (and assuming insoluble surfactant so that the area of compression can be related to the surfactant concentration; see also Eshima *et al.* 2025).

2.3. *Control parameters and initial conditions*

The numerical configuration used here follows the one in Deike *et al.* (2015) used to study capillary effects on breaking waves. As discussed in the Introduction, the problem can be defined by a set of dimensionless parameters: the initial wave slope ak (going from non-breaking to breaking waves), the wave Reynolds and Bond numbers, and the air–water density and viscosity ratios ($\rho_a/\rho_w = 1/850$ and $\mu_a/\mu_w = 1.96 \times 10^{-2}$). We will investigate the influence of Re, Bo and ak on the wave patterns and dynamics for various surfactant contamination measured by the parameter β.

Following Deike *et al.* (2015), the wave is initialised using a nonlinear potential flow solution Φ_0 with corresponding free-surface elevation η_0, based on a third-order Stokes wave approximation (Lamb 1924). This set-up provides both the initial wave profile and the associated water velocity field, so that all cases are initialised consistently, ensuring that the comparative trends across different Bo and β remain robust. We note the work from Shelton & Trinh (2022) that included the effect of surface tension to compute Stokes waves with surface tension at high steepness. The wave propagates in a periodic domain with free-slip boundary conditions at the top and bottom walls. The wavelength is equal to the domain length, and the water depth is set to $h/\lambda = 1/2$, ensuring that depth effects on wave evolution are negligible, consistent with Deike *et al.* (2015).

In the presence of surfactants, two main non-dimensional parameters β and $\Delta\sigma_\infty$ are introduced from the EOS (2.5). We explore a broad parameter space with $0.005 \leqslant \beta \leqslant 1$ for $10^1 \leqslant Bo \leqslant 10^3$, $ak = 0.2$, 0.25, 0.3, 0.35, and $Re = 10^4$, 4×10^4, 10^5, with $\Delta\sigma_\infty$ fixed as 0.5. Since the surfactant transport in our study is dominated by advection, Pe should be sufficiently high so that further increases have a negligible influence on the results; Pe is fixed at 40 based on the convergence test for increasing Pe shown in Appendix A.

All simulations run up to $t = 2T_0$, where $T_0 = 2\pi/\sqrt{gk}$ is the linear wave period derived from the gravity wave linear dispersion relation. The wave period based on the full gravity-capillary wave dispersion relation varies slightly with Bo, but the variation is minimal for the range of Bo considered here. Variations due to nonlinear effects are also small (see Deike *et al.* 2015).

Over this time, the formation of parasitic capillaries or spilling breaking waves can be observed and characterised, together with the associated energy dissipation.

To ensure numerical accuracy, grid convergence tests are performed for various combinations of Bo and β, as shown in Appendix A. We examine both the instantaneous wave shape (after one wave period) and the time evolution of the total energy budget at grid resolutions $L = 8$, 9 and 10, where L is the maximum level of adaptive refinement. The results show convergence in both interface dynamics and energy evolution. Based on this analysis, we adopt $L = 9$ (corresponding to $2^9 = 512$ grid cells per wavelength) as the standard resolution for all cases, except for $Re = 10^5$, where $L = 10$ is used to resolve the thinner boundary layers associated with higher Reynolds numbers.

We focus in this paper on two-dimensional simulations of surfactant effects on surface waves in order to span a wide parameter range, allowing us to rigorously investigate the effect of the various non-dimensional parameters (wave parameters Bo, Re and ak, as well as surfactant parameter β), together with grid resolution verification. These simulations will permit us to discuss the transition in dynamics from gravity waves to parasitic capillary waves, as well as the transition from breaking to non-breaking. Energy dissipation in these various regimes is then quantified. We performed in total

https://doi.org/10.1017/jfm.2026.11260 Published online by Cambridge University Press

ak	Re	Bo	β	Total CPU hours
0.2−0.35	10^4-10^5	10^1-10^3	0.005−1	4×10^4

Table 1. Ranges of control parameters used in the simulations.

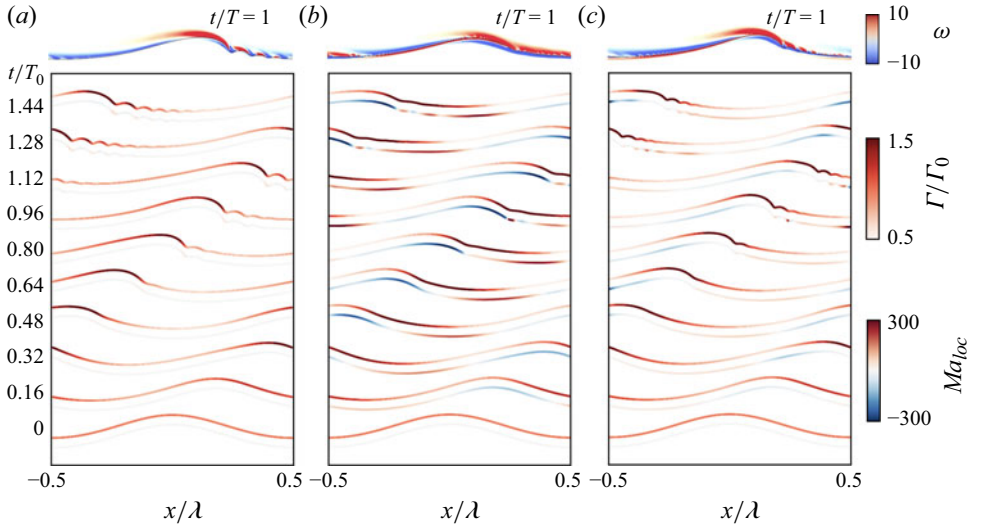


Figure 2. Effect of surfactant on gravity-capillary waves at low Bond number for $ak=0.3$, $Re=4\times10^4$, $Bo=10$ and (*a*) $\beta=0.005$, (*b*) $\beta=0.3$ and (*c*) $\beta=1$. The top images show the instantaneous vorticity field at $t/T=1$. The time evolution (from bottom to top, starting at $t/T=0$ and then at intervals $t/T=0.16$) of the interface is shown ,together with a colour map of the upper surface representing the distribution of normalised surfactant concentration, and the colour map of the lower surface represents the local Marangoni number Ma_{loc}.

400 simulations for a total cost of 40 000 CPU hours, summarised in table 1. Three-dimensional simulations would be a natural next step, allowing us to explore transverse Marangoni effects, bubble entrainment and break-up, and drop formation, to name a few, in targeted regimes of parameters, informed by the present study. The code for this work is available online (https://basilisk.fr/sandbox/ryang/surfactant/).

3. Effect of surfactant on the flow structures

We discuss the effects of surfactants on the flow structure for gravity capillary waves of increasing initial wave slope, going from gravity waves to parasitic capillary waves, and eventually to spilling breakers when increasing the wave slope.

3.1. *Non-monotonic suppression of parasitic capillary waves*

We first examine the evolution of the wave interface at low Bond number $Bo=10$ and slope below the breaking threshold $ak=0.3$, with different values of the surfactant parameter β. Figure 2 shows the time evolution of the interface, the surfactant concentration at the interface, and the local Marangoni number (defined in (1.2)).

For a small value $\beta=0.005$, the influence of surfactants is weak, and the initial wave profile corresponds to a clean gravity-capillary wave. As the wave progresses, parasitic

https://doi.org/10.1017/jfm.2026.11260 Published online by Cambridge University Press

capillary waves gradually emerge on the forward face of the main wave, consistent with prior observations (Deike *et al.* 2015) (figure 2*a*). Positive vorticity is located at the crests of both the main wave and the parasitic waves, while negative vorticity appears near the troughs. These parasitic capillary waves result from the localised high curvature at the wave crest, where surface tension effects are dominant, and are finally damped by viscosity (Fedorov & Melville 1998). These parasitic capillaries are also found to significantly enhance dissipation (Fedorov & Melville 1998; Melville & Fedorov 2015).

The colour fields along the interface in the figure represent the normalised surfactant concentration and the normalised local surface tension gradient to visualise the influence of Marangoni forcing. The surfactant concentration illustrates the redistribution of surfactants from an initially uniform state. As time evolves, surfactants accumulate at the front face of the wave crest where parasitic waves originate. From the surfactant concentration and the EOS, the surface tension gradient can be calculated and indicates both the direction and strength of the Marangoni force, which is weak due to the low value of the parameter β (effectively a very low surfactant concentration).

As β increases (figure 2(*b*), $\beta = 0.3$), surfactant effects become more pronounced. The formation of parasitic waves is nearly fully suppressed. This damping effect is consistent with previous experimental findings that show suppression of parasitic ripples with surfactant (Xu & Perlin 2023). The surfactant continues to accumulate at the front face of the crest, where it decreases the local surface tension. The non-uniform distribution of surfactant also induces stronger surface tension gradients compared to lower β, which is shown in the colour field of surface tension gradients. It acts opposite to the direction of surfactant accumulation, and tends to stretch and smooth the wave crest. Correspondingly, near-surface vorticity intensifies compared to the $\beta = 0.005$ case, due to enhanced Marangoni flow, with the magnitude of the local Marangoni number being much higher.

For even larger values of β (figure 2(*c*), $\beta = 1$), parasitic capillary waves recur, but with reduced amplitude compared to the low-β case ($\beta = 0.005$). The surfactant again accumulates at both the main wave crest and the crests of the parasitic waves. However, the surface tension gradient is weaker than in the intermediate case ($\beta = 0.3$), indicating a weaker Marangoni effect. Similarly, the vorticity field is stronger than in the low-β case, but weaker than in the intermediate-β case, where parasitic suppression is most pronounced.

Because the surfactant concentration reaches local maxima at the crests of both the main wave and the parasitic ripples, and gradually decays away from these regions, the resulting surface tension distribution varies accordingly. The associated surface tension gradients drive opposing Marangoni flows on either side of each ripple, giving rise to the observed spatial variations in Ma_{loc}. This variation appears as alternating blue–red spikes at the parasitic ripples in figure 2(*a–c*).

This non-monotonic behaviour in the surfactant parameter β suggests a complex interaction between surfactant transport, Marangoni forcing and wave steepening, which we now analyse. Figure 3 shows the evolution of the wave interface at a larger Bond number, $Bo = 200$, and $ak = 0.3$ for varying values of β. In this high-Bo regime, gravity dominates the wave dynamics. Similar to the $Bo = 10$ cases, surfactant accumulates near the front of the wave crest, and the colour fields reveal a non-monotonic dependence of the surface tension gradient magnitude on β. The wave surface at $\beta = 1$ remains smooth during time evolution, characteristic of a pure gravity wave, while for lower values of β, small ripples can still be observed near the crest. The addition of surfactant introduces localised surface tension gradients that generate Marangoni shear along the crest. This shear can locally destabilise the interface and enhance wave steepening, particularly at

https://doi.org/10.1017/jfm.2026.11260 Published online by Cambridge University Press

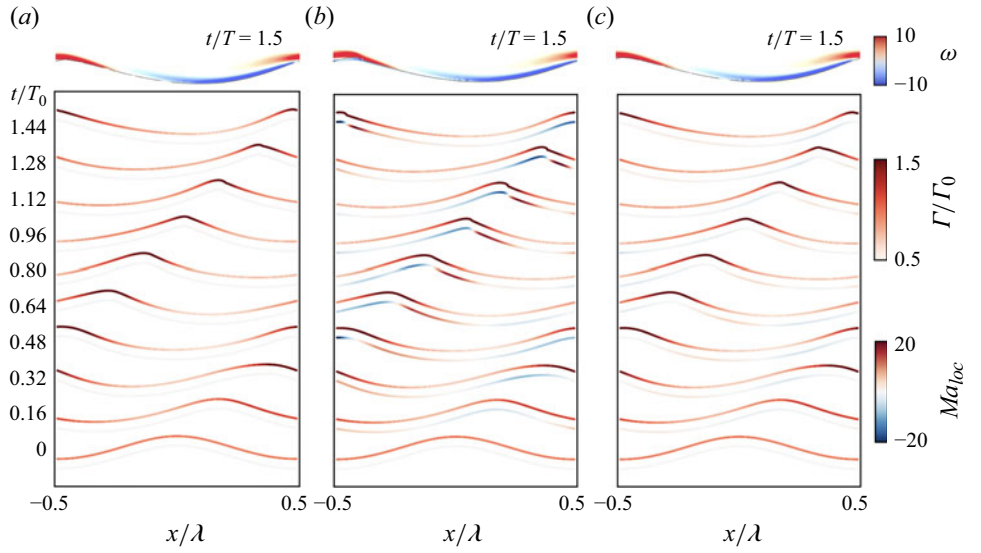


Figure 3. The instantaneous vorticity field and the time evolution of the interface for $ak = 0.3$, $Re = 4 \times 10^4$, $Bo = 200$ and (*a*) $\beta = 0.005$, (*b*) $\beta = 0.3$ and (*c*) $\beta = 1$. The top images show the instantaneous vorticity field at $t/T = 1.5$. The time evolution (from bottom to top, starting at $t/T = 0$ and then at intervals $t/T = 0.16$) of the interface is shown together with a colour map of the upper surface representing the distribution of normalised surfactant concentration, and the colour map of the lower surface represents the local Marangoni number Ma_{loc}.

moderately high Bo, where Marangoni stresses remain dynamically relevant despite the dominance of gravity. Nevertheless, the overall wave evolution is only weakly influenced by the presence of surfactant at high Bo. It was expected that the Marangoni effect is less pronounced in this high-Bo regime, which is highlighted by the relatively low local Marangoni numbers observed.

3.2. *Non-monotonic suppression on spilling breakers at higher ak*

We now consider the effect of β for larger $ak = 0.35$, which can lead to wave breaking (Deike *et al.* 2015). The different wave breaking regimes are identified using slope-based criteria following Deike *et al.* (2015): a spilling breaker is defined by the appearance of a vertical segment in the interface profile (i.e. a $-90°$ slope), while a plunging breaker characterised by wave overturning is identified by the presence of both vertical and horizontal segments (i.e. a $-180°$ configuration), as illustrated in figure 4.

Figure 5(*a–c*) show the time evolution of the wave interface for $ak = 0.35$ and $Bo = 40$ at different values of β. These snapshots illustrate a transition from spilling breakers to parasitic capillary waves, and then back to spilling breakers as β increases. This transition can be seen from the time evolution of interface shapes shown in figure 5(*a–c*) and the slopes indicated by dashed lines at approximately one wave period (the 7th wave profile): at low and high β, the leading wave crest is taller and sharper, while at intermediate β, it becomes lower and broader, indicating the suppression of wave breaking. In figure 5(*b*,*c*), we see a transition from parasitic capillary wave to spilling breaker (vertical interface exceeds 90°, with the spilling associated with more mixing and higher wave slope). Higher Bo will lead to plunging breakers following the criteria from figure 4(*d*). Note that at a later stage, the single wave crest splits into more crests, which is a representative spilling breaker as the bulge near the crest releases and transitions into a train of surface ripples

https://doi.org/10.1017/jfm.2026.11260 Published online by Cambridge University Press

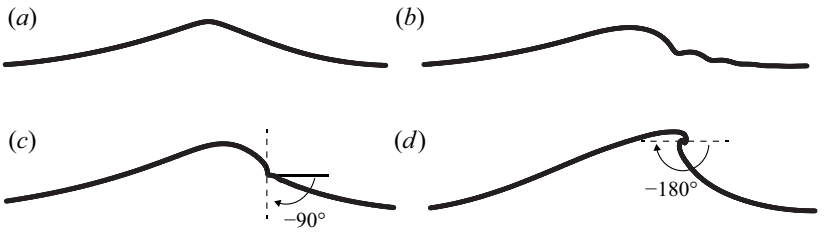


Figure 4. Illustration of typical wave shapes and breaking criteria: (*a*) gravity wave; (*b*) parasitic capillary wave; (*c*) spilling breaker with a vertical segment ($-90°$); (*d*) plunging breaker with both vertical and horizontal segments ($-180°$).

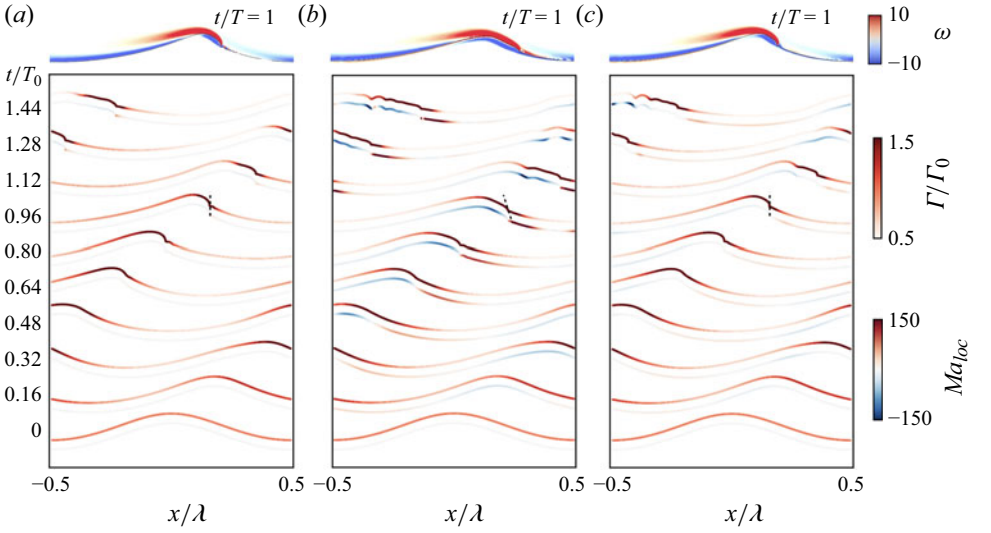


Figure 5. The instantaneous vorticity field and time evolution of the interface for $ak = 0.35$, $Bo = 40$ and (*a*) $\beta = 0.005$, (*b*) $\beta = 0.3$, (*c*) $\beta = 1$. Here, (*a*) and (*c*) are spilling breakers, and (*b*) is parasitic capillary waves following the crest shape criteria from Deike *et al.* (2015). The top images show the instantaneous vorticity field at $t/T = 1$. The time evolution (from bottom to top, starting at $t/T = 0$ and then at intervals $t/T = 0.16$) of the interface is shown together with a colour map of the upper surface representing the distribution of normalised surfactant concentration, and the colour map of the lower surface represents local Marangoni number Ma_{loc}.

(Liu & Duncan 2006). Surfactant accumulation on the front face could also enhance this deformation by reducing the local surface tension.

The corresponding surfactant concentration distributions and local surface tension gradients for these cases are also shown in the colour field. These results are qualitatively similar to those observed for $ak = 0.3$, except that the surfactant concentration is more focused compared to the non-breaking case due to stronger surface compression.

3.3. *Mean square slope evolution and local Marangoni number*

We have observed a modification of the dynamics at intermediate values of β, leading to the suppression of parasitic capillary waves or breaking event due to strong Marangoni stresses, with such effects modulated by the relative strength of gravity and surface tension (Bond number) and wave slope.

To quantify the influence of surfactants on wave dynamics, we examine the time evolution of the mean square slope (s^2) of the wave interface. Figure 6(*a*) shows the

https://doi.org/10.1017/jfm.2026.11260 Published online by Cambridge University Press

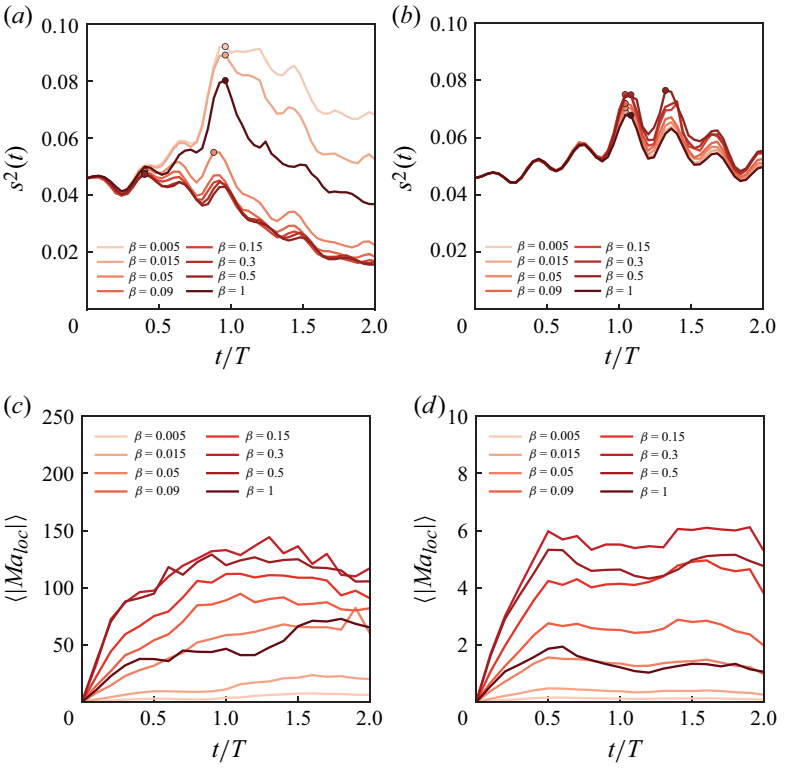


Figure 6. (*a*,*b*) The evolution s^2 for $ak = 0.3$ and (*a*) $Bo = 10$, (*b*) $Bo = 200$, with different values of β colour-coded. The points represent the global maxima. (*c*,*d*) The evolution of the spatially averaged local Marangoni number $\langle|Ma_{loc}|\rangle$ for $ak = 0.3$ and (*c*) $Bo = 10$, (*d*) $Bo = 200$, with different β.

evolution of s^2 for various values of β at low Bo ($Bo = 10$). At low β, s^2 initially increases during the first wave period due to the emergence of parasitic capillary waves, then gradually decays as the viscosity dissipates energy. In contrast, for intermediate values of β, s^2 decreases nearly monotonically over time, reflecting the suppression of parasitic capillaries under strong Marangoni forcing. At even higher values of β, $s^2(t)$ again exhibits an initial increase followed by decay – indicating the reappearance of parasitic capillaries. For the high-Bo case ($Bo = 200$), as shown in figure 6(*b*), the effect of β is negligible, consistent with the interface evolution in figure 3.

Furthermore, we examine the time evolution of the spatially averaged local Marangoni number $\langle|Ma_{loc}|\rangle$, defined in (1.2), at $Bo = 10$ and 200, as shown in figure 6(*c*,*d*). The results show a non-monotonic but opposite evolution trend with β compared to the trend of s^2. As β increases, $\langle|Ma_{loc}|\rangle$ first increases and then decreases, consistent with our observation in figures 2 and 3. The trends are similar for different Bo but with different magnitudes – a much lower magnitude at higher Bo.

Then we compute the time-averaged $\overline{s^2}$ and time-averaged local Marangoni number $\overline{\langle Ma_{loc}\rangle}$, where the bar represents time averaging over the interval $t/T_0 \in [0.8, 1.2]$, corresponding to the period when parasitic capillary waves or breaking waves begin to develop, which is the primary focus of our analysis, while significant wave damping has already occurred after that. Figure 7(*a*) present $\overline{s^2}$ versus $\overline{\langle|Ma_{loc}|\rangle}$ for all different Bo at $ak = 0.3$, with the circles representing each simulation case. They reveal the dependence of surface deformation on Marangoni forcing, with a strong modulation by the Bond

https://doi.org/10.1017/jfm.2026.11260 Published online by Cambridge University Press

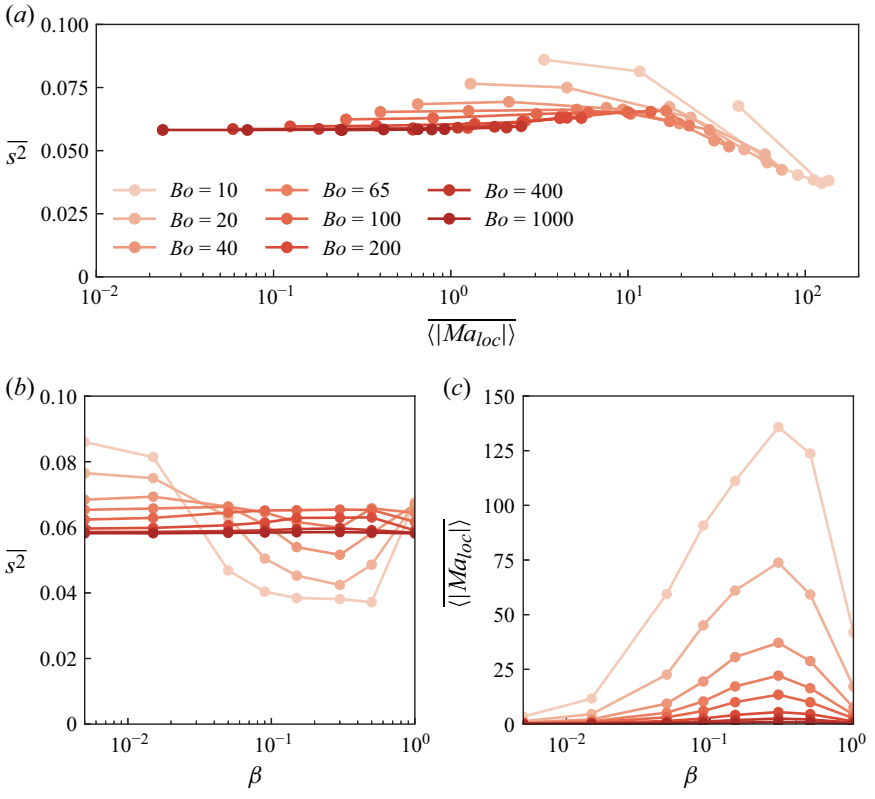


Figure 7. (*a*) Time-averaged $\overline{s^2}$ as a function of time-averaged $\overline{\langle|Ma_{loc}|\rangle}$ with the colour map for different *Bo* at $ak = 0.3$. Plots of (*b*) $\overline{s^2}$ and (*c*) $\overline{\langle|Ma_{loc}|\rangle}$ as functions of β with different *Bo* at $ak = 0.3$.

number, and a clear collapse at high $\overline{\langle|Ma_{loc}|\rangle}$, which shows that the surface roughness quantified by the mean square slope is dominated by Marangoni forcing. Figure 7(*b*,*c*) show both $\overline{s^2}$ and $\overline{\langle|Ma_{loc}|\rangle}$ as functions of β with different *Bo* for $ak = 0.3$. They show non-monotonic trends of $\overline{s^2}$ and $\overline{\langle|Ma_{loc}|\rangle}$ with β, with again a strong modulation by the Bond number: when capillary effects are stronger, the variations in Marangoni effects and roughness are stronger with the surfactant parameter β.

4. Phase diagram

We now characterise systematically the different wave regimes as a function of the controling parameters, the initial wave slope ak, the Bond number, and the surfactant parameter. The different wave regimes (gravity wave, parasitic capillary waves, spilling breakers) are identified and characterised by s^2 and the local Marangoni numbers.

4.1. *From gravity to parasitic capillary waves*

Figure 8(*a*) presents the phase diagram with the symbols colour-coded with $\overline{\langle|Ma_{loc}|\rangle}$, which shows a region of enhanced Marangoni forcing at low *Bo* and intermediate β. We observe three wave regimes following the wave patterns described in figure 4: regime I of gravity waves (square markers), at mostly high Bond number; regime II of parasitic capillary waves (circle markers); and regime III at low Bond number and intermediate β

https://doi.org/10.1017/jfm.2026.11260 Published online by Cambridge University Press

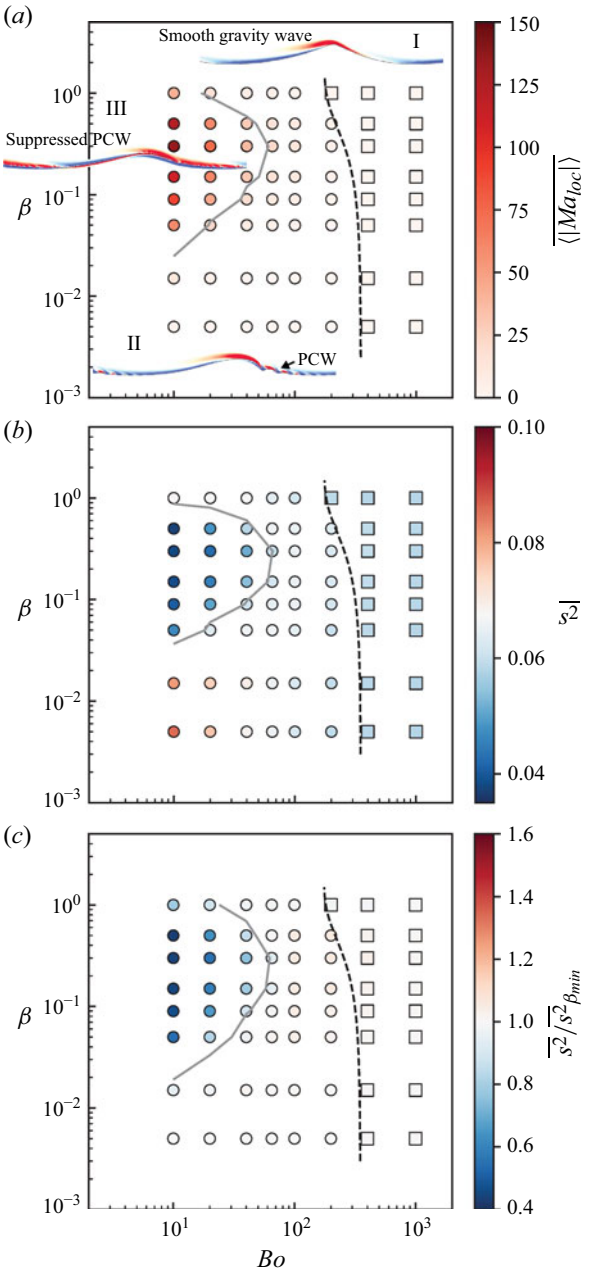


Figure 8. The phase diagrams of wave patterns colour-coded by (*a*) $\overline{\langle |Ma_{loc}| \rangle}$, (*b*) $\overline{s^2}$, and (*c*) normalised $\overline{s^2}/\overline{s^2}_{\beta_{min}}$, all for $ak = 0.3$. The squares represents the pure gravity waves, and the circles represents the parasitic capillary waves (PCW). In (*a*), the grey solid line represents the contour $\overline{\langle |Ma_{loc}| \rangle} = 25$ from simulations. In (*b*), the grey solid line represents the contour $\overline{s^2} = 0.06$. In (*c*), the grey solid line represents the contour $\overline{s^2}/\overline{s^2}_{\beta_{min}} = 0.9$. The dashed lines represent the curve $Bo_c(\beta)$ from (4.3), with $Bo_c(0) = 350$. The snapshots I, II and III represent the typical wave shapes in each regime, which can be briefly described as smooth gravity wave, PCW, and suppressed PCW.

https://doi.org/10.1017/jfm.2026.11260 Published online by Cambridge University Press

where parasitic capillary waves are suppressed by Marangoni effects (also circle markers, but with high values of Marangoni number). The classification is based on the presence of surface slope change, determined by a threshold on the local interface gradient.

Regime I occurs at high Bo, and the transition from regime II to regime I agrees with the clean-water case when β is small (Deike *et al.* 2015) – see more details in Appendix B – but shifts to lower Bond numbers as β increases. We plot a contour line for $\overline{\langle|Ma_{loc}|\rangle} = 25$, which indicates the transition to regime III. Since the transition of surfactant effects is a gradual and continuous process rather than a sharp boundary, the threshold value $\overline{\langle|Ma_{loc}|\rangle} = 25$ was chosen as a representative indicator to visualise the onset of strong Marangoni effects in the phase diagram. The contours serve as visual indicators to identify when the Marangoni effect becomes dominant.

To quantify the wave shape for different control parameters, we plot the phase diagram with $\overline{s^2}$ colour-coded in (Bo, β) space at $ak = 0.3$, shown in figure 8(b). The results also reveal that the influence of β on $\overline{s^2}$ is most pronounced at lower Bond numbers, corresponding to the region where $\overline{\langle|Ma_{loc}|\rangle}$ is high. At low Bo, as β increases, $\overline{s^2}$ initially decreases, indicating a strong suppression of parasitic capillaries. Beyond a critical value ($\beta \approx 0.3$), $\overline{s^2}$ begins to increase again with recurrence of parasitic waves. As Bo increases, the sensitivity of $\overline{s^2}$ to variations of β becomes weaker, reflecting the reduced role of surface tension relative to gravity. We also plot a contour line for $\overline{s^2} = 0.06$, which behaves similarly and has a shape comparable to the contour of $\overline{\langle|Ma_{loc}|\rangle}$ in figure 6(a).

To focus on the Marangoni effect and eliminate the effect of Bo, we further show normalised $\overline{s^2}$ by $\overline{s^2}_{\beta_{min}}$ at the same Bo but smallest $\beta = 0.005$, as shown in figure 8(c). This reveals a significant suppression region, as in figure 8(a,b), down to as low as 40 % of the baseline value. We also include a contour line for $\overline{s^2}/\overline{s^2}_{\beta_{min}} = 0.9$, which closely resembles the contour of $\overline{\langle|Ma_{loc}|\rangle}$ and will be used in the following analysis.

More phase diagrams for wave patterns in the (Bo, β) space are shown in figure 9(a–c), with normalised $\overline{s^2}$ colour-coded, exploring different ak and Re. A lower value of the initial wave slope ak is shown in figure 9(a): in comparison to the phase diagram at $ak = 0.3$, $Re = 4 \times 10^4$, the Marangoni effect is weaker in the low-Bo regime, leading to weaker suppression of wave deformation. In contrast, the results in the higher-Re case (figure 9b) exhibit stronger Marangoni forcing, with the wave shape significantly suppressed across a broader range of Bo.

For $ak = 0.35$, figure 9(c) exhibits a more complex behaviour, including cases of wave breaking, denoted as triangle symbols corresponding to spilling breakers, and star symbols for plunging breakers (see figure 4 for geometric definitions). The β-dependent transition between regimes is again observed. At low Bo, strong Marangoni forcing suppresses the formation of parasitic capillary waves. At $Bo = 40$, the Marangoni forcing even inhibits wave breaking, revealing a non-trivial 'spilling breaker–capillary wave–spilling breaker' transition as β increases, which is also shown in figure 5. This transition resembles that reported by Erinin *et al.* (2023) between plunging breakers and spilling breakers when increasing the surfactant concentration. While the specific choice of EOS certainly influences the critical values separating the different regimes, another choice of EOS that would retain the ones discussed experimentally in Erinin *et al.* (2023) (with similar effects on reduction of surface tension, almost linear decay, and then saturation of σ as a function of Γ) would lead to a similar non-monotonic behaviour.

https://doi.org/10.1017/jfm.2026.11260 Published online by Cambridge University Press

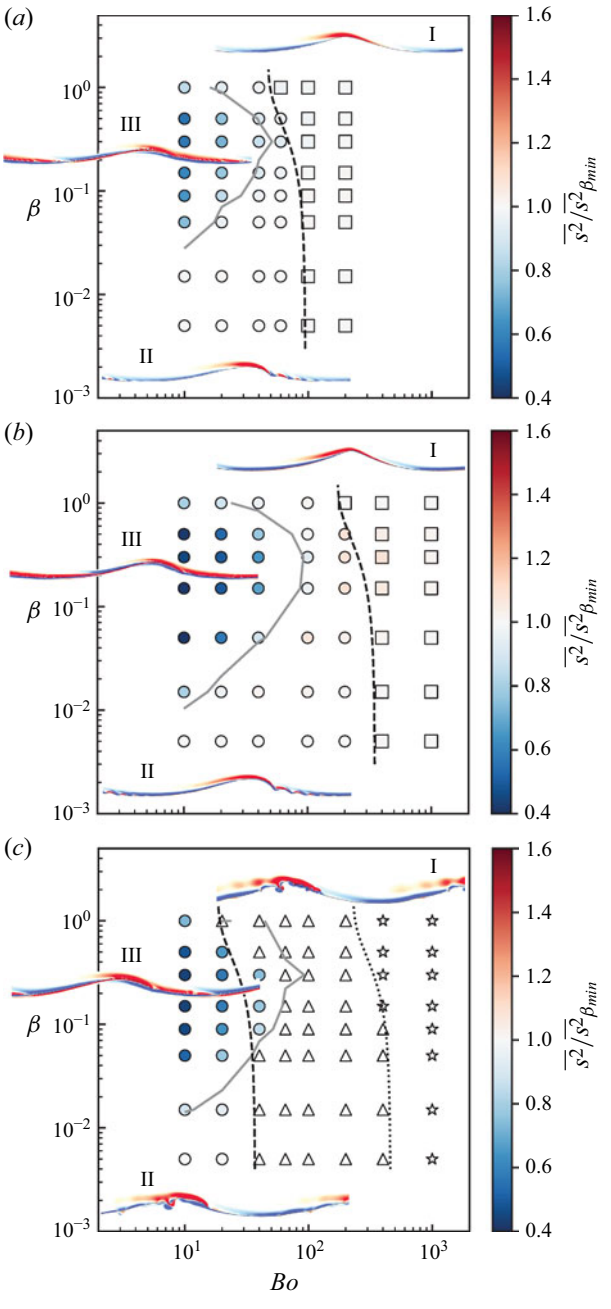


Figure 9. Wave pattern diagrams in the (Bo, β) space with normalised $\overline{s^2}/\overline{s^2}_{\beta_{min}}$ colour-coded, for (*a*) $ak = 0.25$, $Re = 4 \times 10^4$, (*b*) $ak = 0.3$, $Re = 10^5$, and (*c*) $ak = 0.35$, $Re = 4 \times 10^4$, where $\overline{s^2}_{\beta_{min}}$ is the case at the same Bo but smallest $\beta = 0.005$. The grey solid lines represent the contour $\overline{s^2}/\overline{s^2}_{\beta_{min}} = 0.9$. In (*a*,*b*,*c*), circles are parasitic capillary waves, squares are gravity waves, and the dashed lines represent the curve of $Bo_c(\beta)$ from (4.3) for the transition from parasitic capillary wave to gravity wave, with $Bo_c(0) = 95$ in (*a*) and $Bo_c(0) = 350$ in (*b*). In (*c*), triangles are spilling breakers, and stars are plunging breakers. The black dashed and dotted lines represent the curves $Bo_c(\beta)$ for different regime transitions, with $Bo_c(0) = 37$ for the dashed line, and $Bo_c(0) = 460$ for the dotted line, which is in good agreement with the transitions in previous study of wave breaking in clean water (Deike *et al.* 2015); see Appendix B.

https://doi.org/10.1017/jfm.2026.11260 Published online by Cambridge University Press

4.2. *Scaling the boundaries*

In this subsection, we provide a physical explanation for the mechanisms underlying the effects of surfactants on wave dynamics, which includes two main contributions: (i) the reduction of local surface tension due to the presence of surfactants; and (ii) the generation of Marangoni flows driven by surfactant concentration gradients, which act as additional forcing terms in the system. Consequently, two main outcomes are observed as β varies: (1) a shift in the wave regime from capillary-dominated to gravity-dominated behaviour at high Bo, and (2) a non-monotonic variation in normalised $\overline{s^2}$, particularly at low Bo.

We first focus on the regime transition. At high Bo, the effect of Marangoni forcing becomes less significant, given the inverse dependence of Ma on Bo. In this regime, the dominant mechanism is the reduction of surface tension by surfactants. While the input Bo is defined using the clean surface tension σ_c, the actual surface tension $\sigma(\Gamma_0)$ depends on the surfactant distribution even for a uniform concentration $\Gamma = \Gamma_0$, as specified by (2.5). Therefore, we introduce an effective Bond number Bo_{eff} that accounts for the surfactant-modified surface tension, which is defined as

$$Bo_{eff}(\beta) = \frac{\Delta\rho\, g}{\sigma(\Gamma_0)k^2} = Bo\frac{\sigma_c}{\sigma(\Gamma_0)} = \frac{Bo}{1 - \Delta\sigma_\infty \tanh(\beta/\Delta\sigma_\infty)}. \tag{4.1}$$

To characterise the transition between capillary and gravity wave regimes, we define a critical Bond number $Bo_c(\beta)$ as a function of β. When no surfactant is present ($\beta = 0$), the critical value reduces to a constant $Bo_c(0)$. The regime transition occurs when the effective Bond number equals this critical value, $Bo_{eff}(\beta) = Bo_c(0)$, which gives

$$\frac{Bo_c(\beta)}{1 - \Delta\sigma_\infty \tanh(\beta/\Delta\sigma_\infty)} = Bo_c(0). \tag{4.2}$$

Solving for $Bo_c(\beta)$ in terms of β yields

$$Bo_c(\beta) = Bo_c(0)\,(1 - \Delta\sigma_\infty \tanh(\beta/\Delta\sigma_\infty)). \tag{4.3}$$

The resulting curve for $Bo_c(\beta)$ is plotted as a dashed line in the phase diagrams in figures 8 and 9, and it agrees well with the observed transition boundaries in the phase diagrams. It shows that the observed regime transition is governed primarily by the change in effective Bond number due to surfactant-induced surface tension reduction, rather than by Marangoni stresses.

Then we focus on the non-monotonic dependence of $\overline{s^2}$ on β observed at low Bo, which can be attributed to Marangoni flow induced from non-uniform surfactant distributions. As illustrated in figure 10(*a*,*b*), surfactants tend to accumulate at the front face of the wave crest, driven by surface compression associated with wave motion. We note that a dynamic gas pressure gradient exists on the water surface. This variation mainly reflects the dynamic pressure distribution consistent with the orbital motion, rather than the driver of it. The accumulation region coincides with the typical location where parasitic capillary waves would form in the absence of surfactants. However, the local surfactant accumulation reduces the local surface tension and increases the surface tension gradient. This gradient drives Marangoni flow directed opposite to the wave-induced surface motion, thereby reducing the curvature amplification that would otherwise trigger capillary ripples. In other words, instead of directly flattening the interface through curvature change, the Marangoni stresses damp the local surface velocity gradients responsible for increasing curvature. As a result, the formation of parasitic waves is suppressed.

https://doi.org/10.1017/jfm.2026.11260 Published online by Cambridge University Press

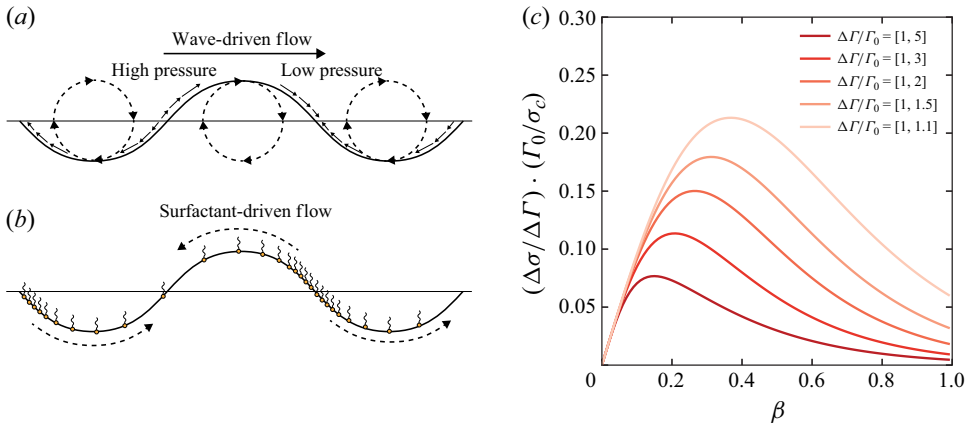


Figure 10. (*a*) Illustration of the wave-driven surface flow pattern without surfactant. (*b*) Illustration of the redistribution of an initially uniform surfactant field due to wave-driven flow and the corresponding surfactant-driven flow. The surfactant concentration is focused at the crest front, which reduces the local surface tension, which further induces Marangoni flow as the dashed arrows. (*c*) The normalised characteristic surface tension gradient as function of β for different compression ranges Γ/Γ_0, calculated from the EOS.

To quantitatively show the non-monotonic dependence of Marangoni forcing on β, we analytically show the dependence of the normalised mean surface tension gradient $(\Delta\sigma/\Delta\Gamma) \cdot (\Gamma_0/\sigma_c)$ on β based on the EOS (2.5) with different ranges of Γ, as shown in figure 10(*c*). Although its magnitude and peak location vary depending on the averaging range of Γ, the non-monotonic trend with respect to β is robust. From our simulations, the maximum local Γ/Γ_0 reaches approximately 2.5 for parasitic capillary waves, and 1.5 for gravity waves. We choose the range $\Gamma/\Gamma_0 \in [1, 2]$ to compute the mean surface tension gradient, which gives the peak of surface tension gradient at $\beta \approx 0.3$. This peak coincides with the strongest suppression of $\overline{s^2}$ and is independent of ak, Bo and Re.

Finally, we focus on the effect of Reynolds number Re, which scales positively with Ma_{local} as in (1.2), and implies that Marangoni effects become stronger at higher Reynolds numbers. We start with the force balance between viscous stress and Marangoni stress:

$$\mu_w \frac{\partial u}{\partial z} \approx \frac{\partial \sigma}{\partial x}. \tag{4.4}$$

Approximating the shear rate by the wave speed c_0 over a surface boundary layer thickness δ, and the surface tension gradient by $\Delta\sigma/\Delta s$, this becomes

$$\mu_w \frac{c_0}{\delta} \approx \frac{\Delta\sigma}{\Delta l}. \tag{4.5}$$

By rearranging, we obtain a dimensionless form

$$\frac{\sigma_c}{\mu_w c_0} \frac{\Delta\sigma}{\Delta l} \frac{\lambda}{\sigma_c} \frac{\delta}{\lambda} \approx \text{const.} \tag{4.6}$$

We further use the scaling $\delta/\lambda \sim Re^{-1/2}$ for boundary layer thickness, which leads to an alternative expression

$$\frac{\Delta\sigma}{\Delta l} \frac{\lambda}{\sigma_c} Bo^{-1} Re^{1/2} \approx \text{const.} \tag{4.7}$$

https://doi.org/10.1017/jfm.2026.11260 Published online by Cambridge University Press

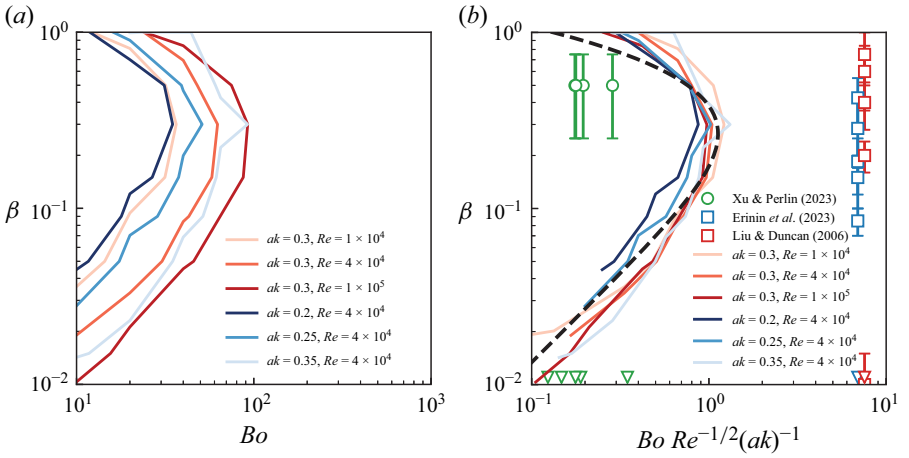


Figure 11. (*a*) The extracted contour lines of $\overline{s^2}/\overline{s^2}_{\beta_{min}} = 0.9$ for different Re and ak. (*b*) The rescaled contour lines by $Bo\,Re^{-1/2}\,(ak)^{-1}$, where the dashed line represents the prediction from (4.9). The green circles represent the experimental data from Xu & Perlin (2023), where suppression of parasitic capillary wave is observed with surfactant. The blue squares represent the experimental data from Erinin *et al.* (2023), where plunging breakers occur for all β. The red squares represent the experimental data from Liu & Duncan (2006), where spilling breakers occur for all β. The triangles show the cases without surfactant ($\beta = 0$).

Furthermore, the surface tension gradient can be written as

$$\frac{\Delta\sigma}{\Delta l} = \frac{\Delta\sigma}{\Delta\Gamma}\frac{\Delta\Gamma}{\Delta l}, \tag{4.8}$$

where $\Delta\sigma/\Delta\Gamma$ is solely determined by β through the EOS, shown in figure 10, while the surfactant concentration gradient $\Delta\Gamma/\Delta l$ is driven by surface advection. Figure 11 shows different values of $\Delta\sigma/\Delta\Gamma = (\sigma(\Gamma_1) - \sigma(\Gamma_2))/(\Gamma_1 - \Gamma_2)$ for typical compression values $\Delta\Gamma/\Gamma_0 = (\Gamma_1 - \Gamma_2)/\Gamma_0$. This advection can be approximately quantified by the transport by the surface velocity, which is proportional to ak for a linear wave. Therefore, the final expression is

$$\frac{\Delta\sigma}{\Delta\Gamma}\frac{\Gamma_0}{\sigma_c}(\beta)\cdot ak\cdot Bo^{-1}\,Re^{1/2} \approx \text{const.} \tag{4.9}$$

To verify the scaling in (4.9), we extract the contour plot of normalised $\overline{s^2} = 0.9$ for all the different ak and Re in figure 11(*a*), since $\overline{s^2}$ is a directly measurable indicator of the surfactant influence on surface roughness, and we have shown that the contours of normalised $\overline{s^2}$ are closely related to the Marangoni forcing. The contour shifts towards higher Bo as Re and ak increase, indicating a broader region influenced by Marangoni stresses at higher Re and ak, consistent with (4.9).

We rescale the horizontal axis of the phase diagram using $Bo\,Re^{-1/2}\,(ak)^{-1}$ based on the scaling analysis from (4.9). As shown in figure 11(*b*), this rescaling collapses the threshold contours across different Re and ak, and is well predicted by (4.9) represented by the dashed line. At small β (<0.1), the EOS reduces to an approximately linear relation, and the dashed line exhibits the same behaviour. At large β, the dashed line is governed by the full nonlinear EOS. The experimental results of Xu & Perlin (2023) also show suppression of parasitic capillary waves in the presence of surfactant, indicated by the green circles in figure 11(*b*). In contrast, in the high-Bo regime where Marangoni forcing is weaker, the suppression becomes less pronounced, and plunging breaking persists across

https://doi.org/10.1017/jfm.2026.11260 Published online by Cambridge University Press

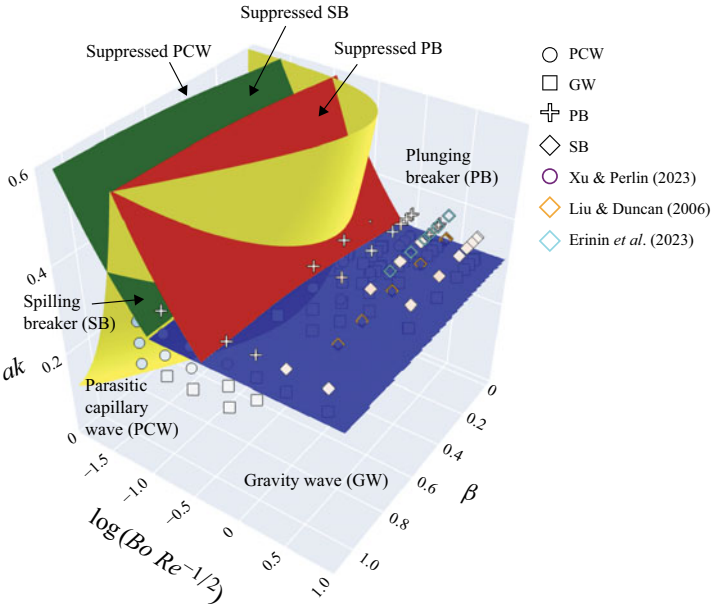


Figure 12. A three-dimensional phase diagram with rescaled $\log(Bo\,Re^{-1/2})$, β and ak. The surfaces with different colours represent the expected transitions among different regimes from (4.3) and (4.9). The different symbols represent our simulation data at different regimes and also experimental data from Liu & Duncan (2006), Xu & Perlin (2023) and Erinin *et al.* (2023), as in figure 11(*b*).

different β. However, the detailed shape of the plunging breaker still changes due to local surfactant accumulation (Erinin *et al.* 2023), as shown by the blue squares in figure 11(*b*).

We further present an expected three-dimensional phase diagram in figure 12 with rescaled $\log(Bo\,Re^{-1/2})$, β and ak. The $\log(Bo\,Re^{-1/2})-ak$ plane at $\beta = 0$ represents the clean-water cases with gravity wave, parasitic capillary wave, spilling breaker and plunging breaker regimes, and corresponding transitions, following Deike *et al.* (2015). As β increases, these transitions shift depending on β. The green and red surfaces corresponds to (4.3), where $Bo_c(0)$ is obtained from $ak = K(1+Bo)^{1/3}$ with $K = 1.12$ for no-breaking to spilling breaker (green surface), and $K = 1.75$ for spilling breaker to plunging breaker (red surface) for the clean-water results from Deike *et al.* (2015). The horizontal blue surface represents the breaking threshold boundary $ak = 0.32$, also from Deike *et al.* (2015). The yellow surface represents (4.9); to its left lies the Marangoni-dominated regime where parasitic capillary waves, spilling breakers or plunging breakers are suppressed depending on the specific location within the diagram. We also include our simulation data and experimental data from Liu & Duncan (2006), Xu & Perlin (2023) and Erinin *et al.* (2023), as in figure 11(*b*), to indicate their locations in this phase diagram (with estimation of β based on the surface tension isotherms reported by Erinin *et al.* 2023).

Note that in real ocean environments or experiments, Re can be more than two orders of magnitude higher than those considered here (Erinin *et al.* 2023); the boundary layer becomes fully turbulent. For certain aspects of the effect of surfactant on waves in the ocean, three-dimensional effects would have to be taken into account. In particular, any study on air entrainment, bubble and droplet formation and statistics would have to account for surfactant effects on three-dimensional dynamics, including spanwise Marangoni effects. Spanwise Marangoni effects can also affect the dynamics of three-dimensional

https://doi.org/10.1017/jfm.2026.11260 Published online by Cambridge University Press

wave patterns. Numerically, as an example, assuming the required resolution scales with the boundary layer thickness as $1/2^L \sim Re^{-1/2}$, reaching $Re \sim 4 \times 10^6$ would demand a minimum grid refinement level $L \approx 13$ and also smaller time steps. This implies that in natural conditions, Marangoni effects might be important for the breaking during the first wave period and extend into higher-Bo regions compared to our simulation results, as illustrated by the experimental work of Erinin *et al.* (2023) and Liu *et al.* (2025). Further exploration of three-dimensional effects would be a natural avenue for future work, targeting only specific ranges of the parameter space given the expected high computational cost.

Longuet-Higgins (1963, 1995) provides a theoretical relationship between the shape of the interface and the formation of parasitic capillary waves (due to capillary pressure resulting in steep waves) and the link with underwater vorticity. In our study, the observed non-monotonic suppression of parasitic capillary waves with increasing β is closely related to the same physical balance, but with the addition of variable surface tension and Marangoni stresses. Incorporating the effects of surfactant-dependent surface tension directly into the Longuet-Higgins analytical model would require reformulating the curvature–pressure balance and the surface boundary conditions to include spatially varying $\sigma(\Gamma)$ and its gradients. The non-monotonic trend observed in our results arises from two competing effects: (i) a reduction in mean surface tension that weakens the capillary restoring force; and (ii) enhanced Marangoni stresses at intermediate β, which oppose surface compression and suppress the parasitic capillary waves. Developing a fully extended analytical model is non-trivial and beyond the present scope, but could be explored in future work.

5. Effect of surfactant on energy dissipation and vorticity

5.1. *Energy dissipation*

We now discuss the effect of surfactant on energy dissipation in the water phase for the various wave regimes. To quantify the total energy dissipation, we consider the total energy $E = E_p + E_k + E_s$, including potential energy E_p, kinetic energy E_k, and surface tension energy E_s, which are calculated as

$$E_k = \frac{1}{2}\int \rho_w \boldsymbol{u}^2 \,\mathrm{d}x\,\mathrm{d}y, \quad E_p = \int \rho_w g y \,\mathrm{d}x\,\mathrm{d}y, \quad E_s = \sigma(l - l_0), \tag{5.1}$$

where l_0 is the surface projection length. We quantify the total energy dissipation by the total energy change from the beginning to the end of the simulation, defined as ΔE.

We investigate the effect of surfactants on the total energy dissipation $\Delta E/E_0$ from the beginning to $t = 2T_0$. Figure 13(*a–c*) show the time evolution of the normalised total energy over two wave periods for $ak = 0.3$ at varying β and Bo. In all cases, the total wave energy decreases in time due to dissipative processes.

At low $Bo = 10$ (figure 13*a*), significant energy dissipation is already visible even at low β due to the presence of parasitic capillary waves (see Deike *et al.* 2015). The effect of β on energy dissipation is then observed to be non-monotonic. For both low and high β values, the energy decays more slowly than at intermediate β values, particularly $\beta \approx 0.3$. This trend contrasts with earlier observations of surface roughness, where rougher interfaces (associated with more prominent parasitic activity at low and high β) are typically expected to exhibit higher dissipation. However, the enhanced energy loss at intermediate β is instead attributed to strong Marangoni flow, which results from larger surface tension gradients. This flow generates increased near-surface shear and vorticity,

https://doi.org/10.1017/jfm.2026.11260 Published online by Cambridge University Press

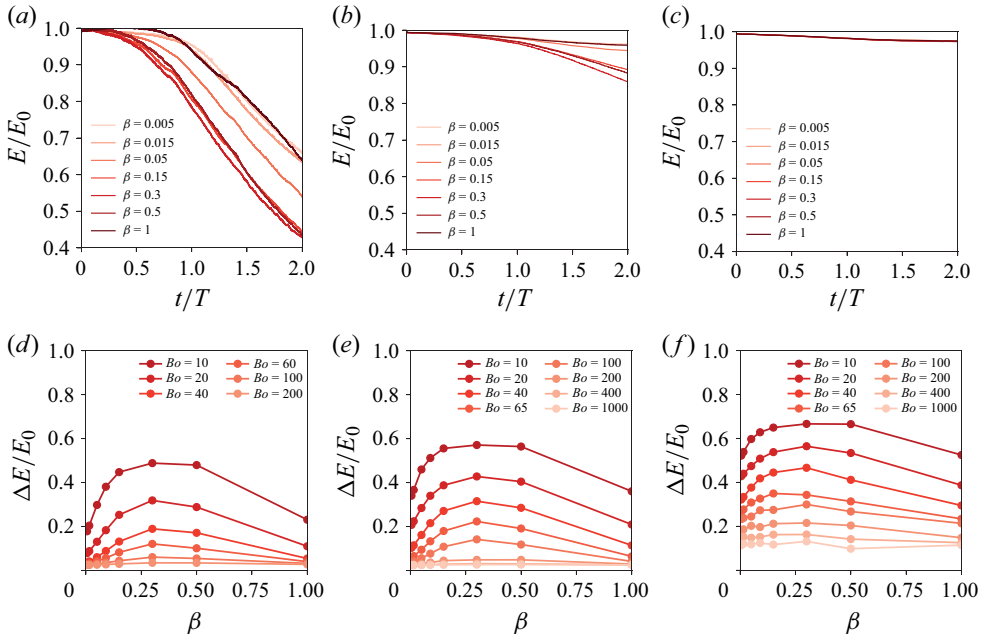


Figure 13. The normalised total energy E/E_0 as a function of time for $ak = 0.3$ and (*a*) $Bo = 10$, (*b*) $Bo = 100$ and (*c*) $Bo = 1000$. The amount of energy decay $\Delta E/E_0$ within $t = 2T$ as a function of β and Bo for (*d*) $ak = 0.25$, (*e*) $ak = 0.3$, (*f*) $ak = 0.35$.

which is shown in the vorticity field snapshot in figure 2(*b*) where $\beta = 0.3$ produces more intense vorticity than other cases.

As Bo increases, shown in figure 13(*b*,*c*) for $Bo = 100$ and $Bo = 1000$, the energy dissipation decreases due to the transition to purely gravity wave with weaker parasitic capillaries. The influence of β on dissipation also becomes weaker, consistent with the weakening of Marangoni effects as Bo increases.

Figure 13(*d–f*) show the total energy loss over two wave periods as functions of both β and Bo for different ak. In all different ak cases, the dissipation exhibits a non-monotonic dependence on β, with the maximum at $\beta \approx 0.3$, corresponding to the analytically strongest Marangoni forcing from EOS. This again supports the conclusion that surfactant-induced surface tension gradients are a key driver of enhanced dissipation at intermediate β values.

Figure 14 shows the total energy dissipation $\Delta E/E_0$ as a function of $\overline{\langle|Ma_{loc}|\rangle}$ at $ak = 0.3$ with different Bo. A positive correlation is observed between $\Delta E/E_0$ and $\overline{\langle|Ma_{loc}|\rangle}$. As Bo increases, $\Delta E/E_0$ and $\overline{\langle|Ma_{loc}|\rangle}$ both decrease. Furthermore, for sufficiently large $\overline{\langle|Ma_{loc}|\rangle}$, the data collapse onto a single curve, indicating that in this regime, the energy dissipation is primarily governed by Marangoni forcing. The same plot for other ak and Re shows similar trends. This analysis demonstrates that as the Marangoni forcing increases, the energy dissipation also always increases for given values of other control parameters (Bo, β or ak), with the initial magnitude that is controlled by the baseline dissipation given by the wave slope and Bond number.

5.2. *Mean surface vorticity*

As mentioned above, Longuet-Higgins (1992) provides a link between the underwater generation of vorticity by nonlinear gravity-capillary waves (parasitic capillary waves) in

https://doi.org/10.1017/jfm.2026.11260 Published online by Cambridge University Press

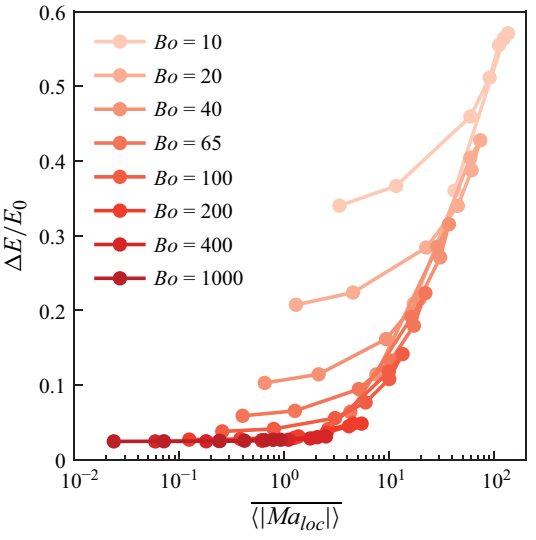


Figure 14. Plots of $\Delta E/E_0$ as functions of $\overline{\langle Ma_{loc} \rangle}$ with different Bo at $ak = 0.3$.

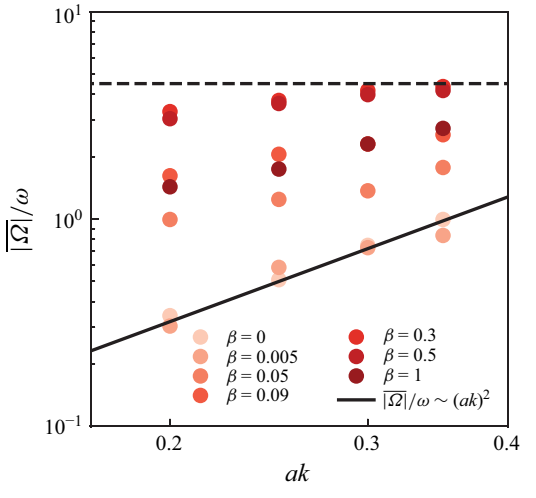


Figure 15. Plots of $\overline{|\Omega|}/\omega$ as functions of ak with different β at $ak = 0.3$ and $Bo = 10$. The solid line shows the $(ak)^2$ scaling (5.2), and the dashed horizontal line shows a relation independent of ak.

the clean case, which was used by Deike *et al.* (2015) to quantify the transition between non-breaking and breaking waves:

$$\Omega = -2(ak)^2\omega, \tag{5.2}$$

where Ω is the surface vorticity, and $\omega = \sqrt{gk + \sigma/\rho k^3}$ is the angular frequency from the linear dispersion relation. We examine how surfactant modifies the mean vorticity magnitude $\overline{|\Omega|}$.

We measure the mean absolute vorticity $\overline{|\Omega|}$ averaged within a viscous boundary layer right below the interface (of thickness $\sim \lambda/\sqrt{Re}$; see Fedorov & Melville 1998; Deike *et al.* 2015). In figure 15, we plot $\overline{|\Omega|}/\omega$ as a function of ak for different values of β. The

https://doi.org/10.1017/jfm.2026.11260 Published online by Cambridge University Press

exact value of $\overline{|\Omega|}/\omega$ depends on the selected averaging region near the surface, but in the clean-water and small-β cases, $\overline{|\Omega|}/\omega$ follows the theoretical $(ak)^2$ scaling predicted by (5.2). As β increases, $\overline{|\Omega|}/\omega$ increases due to the enhanced Marangoni flow, consistent with the enhanced energy dissipation, and it shows a weaker and nearly zero dependence on ak, as Marangoni flow dominates the vorticity at intermediate β, which is independent of ak.

6. Conclusion

In this work, we have systematically investigated the effects of insoluble surfactants on surface wave dynamics across a multi-parameter space characterised by ak, Bo, Re and β. Using direct numerical simulations with a nonlinear equation of state, we explored how surfactant concentration affects wave pattern and surface roughness, including transition from non-breaking to wave breaking modulated by surfactant. The influence of surfactant on parasitic capillary waves is characterised together with energy dissipation. We identified two principal mechanisms by which surfactants influence wave evolution: (i) reduction of local surface tension, which shifts the transition between wave regimes; and (ii) Marangoni stresses induced by surfactant concentration gradients, which act as an additional forcing and tend to suppress surface roughness.

Our results revealed a non-monotonic dependence of $\overline{s^2}$ and $\overline{\langle|Ma_{loc}|\rangle}$ on β in the phase diagrams of different ak and Re, especially at low Bo where Marangoni stresses dominate. The suppression of parasitic capillary waves is directly linked to the strength of the Marangoni forcing, which was found to reach peak value at intermediate $\beta \approx 0.3$. We also observed a β-dependent transition between parasitic capillary waves, gravity waves and breaking wave regimes in all phase diagrams. This transition can be explained and quantitatively predicted using a β-dependent effective Bo, which accounts for local variations in surface tension. Furthermore, we proposed a rescaled parameter $Bo\,Re^{-1/2}\,(ak)^{-1}$, derived from the balance between viscous and Marangoni stresses, which successfully collapses the contours of the Marangoni-dominated regime across different ak and Re.

Finally, the energy budget analysis reveals that surfactants lead to enhanced dissipation at intermediate β, opposite to the trend of suppressed surface roughness. This enhanced dissipation is driven by strong Marangoni flows and the resulting increase in near-surface vorticity. Furthermore, we show that the energy dissipation can be quantified solely by the local Marangoni number $\overline{\langle|Ma_{loc}|\rangle}$ at sufficiently high β as it collapses onto a single curve. Surface vorticity follows the theoretical scaling from Longuet-Higgins (1992) for small-β cases. As β increases, surface vorticity increases due to enhanced Marangoni flow, consistent with the trend of energy dissipation.

Funding. This work is supported by the National Science Foundation under grant 2318816 to L.D. (Physical oceanography), and the NASA Ocean Vector Winds Science Team, grant 80NSSC23K0983 to L.D.

Declaration of interests. The authors report no conflict of interest.

Appendix A. Grid convergence and sensitivity to Péclet number and other numerical parameters

We examine both the instantaneous wave shape (after one wave period) and the time evolution of the total energy budget at grid resolutions $L = 8, 9, 10$ for $ak = 0.3$, $Re = 4 \times 10^4$ with different Bo and β, as shown in figure 16. All results show good convergence in both the instantaneous wave shape and the energy budget from $L = 9$.

https://doi.org/10.1017/jfm.2026.11260 Published online by Cambridge University Press

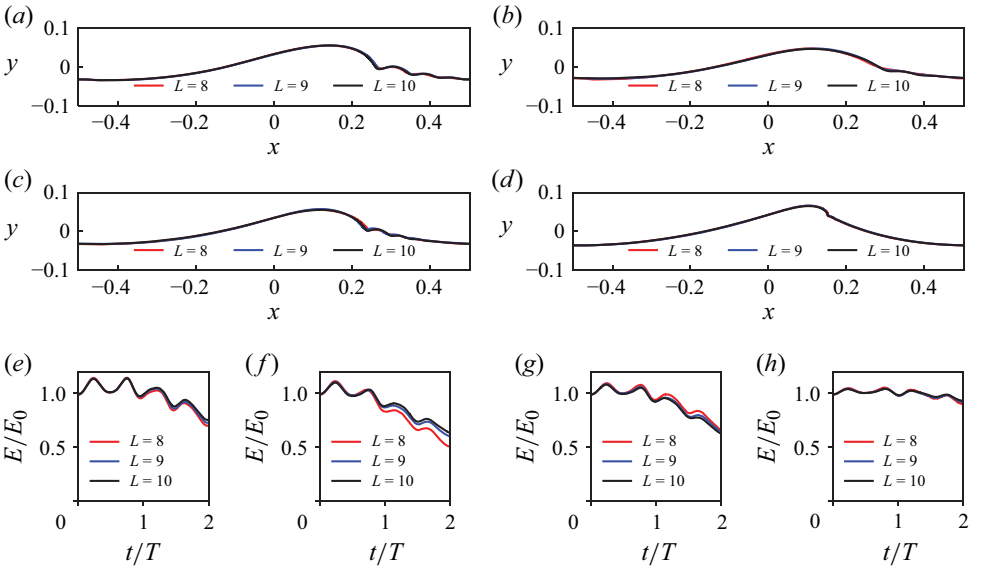


Figure 16. The instantaneous wave interface after one wave period with different resolutions. The corresponding control parameters are $ak = 0.3$ and (*a*) $Bo = 10$, $\beta = 0.005$, (*b*) $Bo = 10$, $\beta = 0.3$, (*c*) $Bo = 10$, $\beta = 1$, (*d*) $Bo = 100$, $\beta = 0.3$. (*e–h*) Corresponding total energy budget evolution.

We also test the effect of Pe on the wave shape and energy budget for a specific case with $ak = 0.3$, $Re = 4 \times 10^4$, $Bo = 10$, $\beta = 0.3$, as shown in figure 17(*a*,*b*). The results show good convergence for increasing Pe from $Pe = 40$.

There are two numerical parameters in the phase field model, namely the phase field thickness ε, and the velocity scale parameter ζ, where ε is typically set at approximately the minimum resolution to ensure that the interface is sharp enough, and ζ for the phase field velocity scale is required to be $\zeta \geqslant |\boldsymbol{u}|_{max}$. We test for different values for $\varepsilon = [0.75, 1, 2]\Delta x_{min}$ and $\zeta = [1, 1.1, 2]|\boldsymbol{u}|_{max}$, as shown in figure 17(*c–f*). Both show insensitivity to the wave shape and energy budget.

Appendix B. Comparison to the regime transition of clean-water cases

Two non-dimensional parameters are critical to the breaking dynamics: wave steepness ak, and the Bond number Bo. Deike *et al.* (2015) showed a wave regime diagram with boundaries between different types of breaking waves for clean water based on the numerical results. The figure is re-plotted here as figure 18. The transition points of different regimes at $ak = 0.35$ and minimum surfactant $\beta = 0.005$ observed in this study are added to the diagram, shown as filled green circles, which agrees with the phase diagram from Deike *et al.* (2015).

https://doi.org/10.1017/jfm.2026.11260 Published online by Cambridge University Press

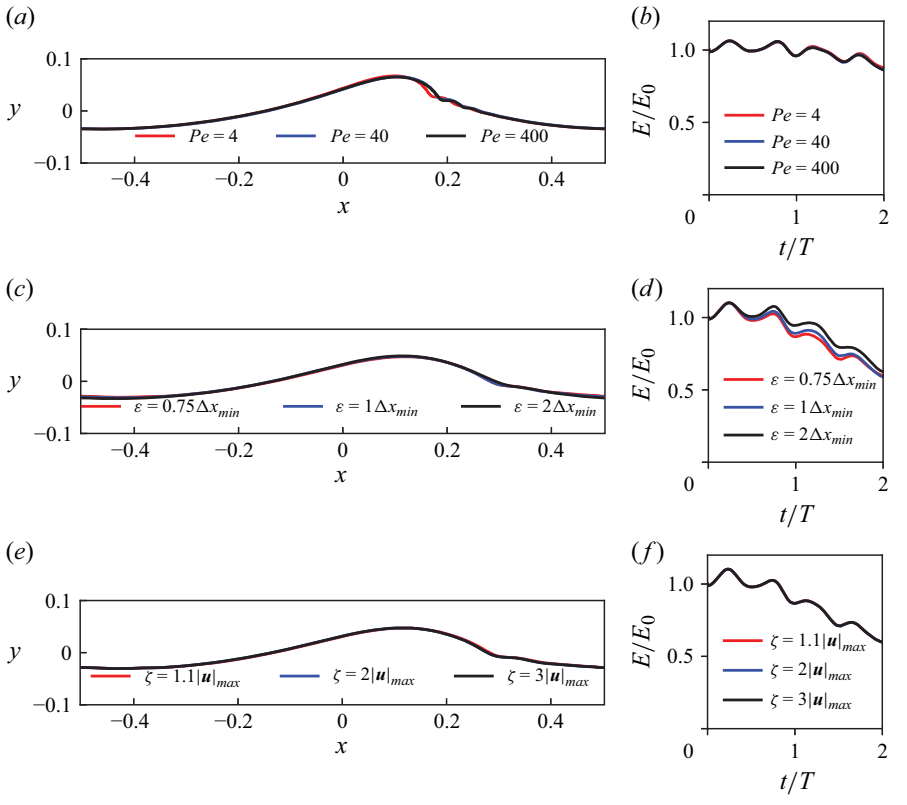


Figure 17. (*a*) The instantaneous wave interface after one wave period, and (*b*) the total energy evolution with different Pe and $ak = 0.3,\ Bo = 10,\ \beta = 0.3$. (*c*) The instantaneous wave interface after one wave period, and (*d*) the total energy evolution with different phase field interface thickness ε and $ak = 0.3,\ Bo = 10,\ \beta = 0.3$. (*e*) The instantaneous wave interface after one wave period, and (*f*) the total energy evolution with different values of ζ and $ak = 0.3,\ Bo = 10,\ \beta = 0.3$.

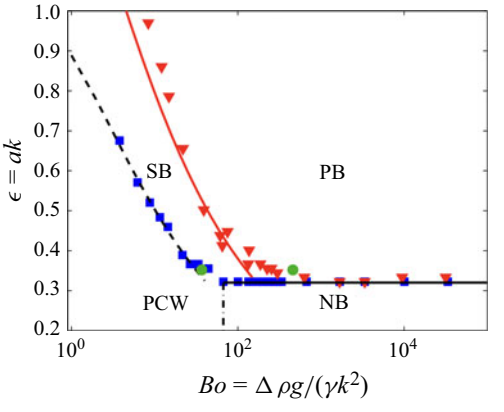


Figure 18. Wave regime diagram (Bo, ak) for clean water. The boundaries between the wave regimes are obtained numerically in Deike *et al.* (2015). PB indicates plunging breakers; SB indicates spilling breakers; PCW indicates parasitic capillary waves; NB indicates non-breaking gravity waves. Green circles represent the transition points from PCW to SB, and SB to PB, at $ak = 0.35$ and $\beta = 0.005$ in this study.

https://doi.org/10.1017/jfm.2026.11260 Published online by Cambridge University Press

References

Abu-Al-Saud, M.O., Popinet, S. & Tchelepi, H.A. 2018 A conservative and well-balanced surface tension model. *J. Comput. Phys.* **371**, 896–913.

Alpers, W. & Hühnerfuss, H. 1989 The damping of ocean waves by surface films: a new look at an old problem. *J. Geophys. Res. Oceans* **94** (C5), 6251–6265.

Bell, T., De Bruyn, W., Marandino, C.A., Miller, S., Law, C., Smith, M. & Saltzman, E. 2015 Dimethylsulfide gas transfer coefficients from algal blooms in the Southern Ocean. *Atmos. Chem. Phys.* **15** (4), 1783–1794.

Burrows, S.M., Ogunro, O., Frossard, A., Russell, L.M., Rasch, P.J. & Elliott, S. 2014 A physically based framework for modeling the organic fractionation of sea spray aerosol from bubble film Langmuir equilibria. *Atmos. Chem. Phys.* **14** (24), 13601–13629.

Ceniceros, H.D. 2003 The effects of surfactants on the formation and evolution of capillary waves. *Phys. Fluids* **15** (1), 245–256.

Constante-Amores, C.R., Kahouadji, L., Batchvarov, A., Shin, S., Chergui, J., Juric, D. & Matar, O.K. 2021 Dynamics of a surfactant-laden bubble bursting through an interface. *J. Fluid Mech.* **911**, A57.

Davis, J.R., Thomson, J., Houghton, I.A., Fairall, C.W., Butterworth, B.J., Thompson, E.J., Boer, G., Doyle, J.D. & Moskaitis, J.R. 2025 Ocean surface wave slopes and wind-wave alignment observed in Hurricane Idalia. *J. Geophys. Res. Oceans* **130** (2), e2024JC021814.

Deike, L. 2022 Mass transfer at the ocean–atmosphere interface: the role of wave breaking, droplets, and bubbles. *Annu. Rev. Fluid Mech.* **54** (1), 191–224.

Deike, L., Melville, W.K. & Popinet, S. 2016 Air entrainment and bubble statistics in breaking waves. *J. Fluid Mech.* **801**, 91–129.

Deike, L., Popinet, S. & Melville, W.K. 2015 Capillary effects on wave breaking. *J. Fluid Mech.* **769**, 541–569.

Erinin, M., Liu, C., Liu, X., Mostert, W., Deike, L. & Duncan, J. 2023 The effects of surfactants on plunging breakers. *J. Fluid Mech.* **972**, R5.

Eshima, J., Aurégan, T., Farsoiya, P.K., Popinet, S., Stone, H.A. & Deike, L. 2025 Size amplification of jet drops due to insoluble surfactants. *Phys. Rev. Fluids* **10**, 123604.

Farsoiya, P.K., Popinet, S., Stone, H.A. & Deike, L. 2024 Coupled volume of fluid and phase field method for direct numerical simulation of insoluble surfactant-laden interfacial flows and application to rising bubbles. *Phys. Rev. Fluids* **9** (9), 094004.

Fedorov, A.V. & Melville, W.K. 1998 Nonlinear gravity–capillary waves with forcing and dissipation. *J. Fluid Mech.* **354**, 1–42.

Franklin, B. & Brownrigg, W. 1774 Of the stilling of waves by means of oil. *Phil. Trans. R. Soc. Lond.* **64**, 445–460.

Iafrati, A. 2011 Energy dissipation mechanisms in wave breaking processes: spilling and highly aerated plunging breaking events. *J. Geophys. Res. Oceans* **116** (C7), C07024.

Jain, S.S. 2024 A model for transport of interface-confined scalars and insoluble surfactants in two-phase flows. *J. Comput. Phys.* **515**, 113277.

King, L., Roberts, I.J., Tinel, L. & Carpenter, L.J. 2019 The determination of surfactants at the sea surface. *Ocean Sci. Discuss.* **2019**, 1–30.

Lamb, H. 1924 *Hydrodynamics*. Cambridge University Press.

Liao, Y.-C., Franses, E.I. & Basaran, O.A. 2006 Deformation and breakup of a stretching liquid bridge covered with an insoluble surfactant monolayer. *Phys. Fluids* **18** (2), 022101.

Liu, C., Erinin, M., Liu, X. & Duncan, J. 2025 The effect of surfactants on droplet generation in a plunging breaker. *J. Fluid Mech.* **1009**, A31.

Liu, X. & Duncan, J.H. 2003 The effects of surfactants on spilling breaking waves. *Nature* **421** (6922), 520–523.

Liu, X. & Duncan, J.H. 2006 An experimental study of surfactant effects on spilling breakers. *J. Fluid Mech.* **567**, 433–455.

Liu, X. & Duncan, J.H. 2007 Weakly breaking waves in the presence of surfactant micelles. *Phys. Rev. E* **76** (6), 061201.

Lohse, D. 2023 Surfactants on troubled waters. *J. Fluid Mech.* **976**, F1.

Longuet-Higgins, M.S. 1963 The effect of non-linearities on statistical distributions in the theory of sea waves. *J. Fluid Mech.* **17** (3), 459–480.

Longuet-Higgins, M.S. 1992 Capillary rollers and bores. *J. Fluid Mech.* **240**, 659–679.

Longuet-Higgins, M.S. 1995 Parasitic capillary waves: a direct calculation. *J. Fluid Mech.* **301**, 79–107.

https://doi.org/10.1017/jfm.2026.11260 Published online by Cambridge University Press

LUO, P., ZHANG, J., CAO, Y. & SONG, S. 2024 Simulation of wave scattering over a floating platform in the ocean with a coupled CFD–IBM model. *Theor. Appl. Mech. Lett.* **14** (3), 100516.
MAGDALENA, I., KRISTIANTO, I.J., RIF'ATIN, H.Q., RATNAYAKE, A.S., SAENGSUPAVANICH, C., SOLEKHUDIN, I. & HELMI, M. 2025 Reduction in wave shoaling over a linear transition bottom using a porous medium. *Theor. Appl. Mech. Lett.* **15** (1), 100556.
MANIKANTAN, H. & SQUIRES, T.M. 2020 Surfactant dynamics: hidden variables controlling fluid flows. *J. Fluid Mech.* **892**, P1.
MELVILLE, W.K. & FEDOROV, A.V. 2015 The equilibrium dynamics and statistics of gravity–capillary waves. *J. Fluid Mech.* **767**, 449–466.
MERTENS, J. 2006 Oil on troubled waters: Benjamin Franklin and the honor of Dutch seamen. *Phys. Today* **59** (1), 36–41.
MOSTERT, W., POPINET, S. & DEIKE, L. 2022 High-resolution direct simulation of deep water breaking waves: transition to turbulence, bubbles and droplets production. *J. Fluid Mech.* **942**, A27.
MURADOGLU, M. & TRYGGVASON, G. 2008 A front-tracking method for computation of interfacial flows with soluble surfactants. *J. Comput. Phys.* **227** (4), 2238–2262.
MURADOGLU, M. & TRYGGVASON, G. 2014 Simulations of soluble surfactants in 3-D multiphase flow. *J. Comput. Phys.* **274**, 737–757.
NÉEL, B. & DEIKE, L. 2021 Collective bursting of free-surface bubbles, and the role of surface contamination. *J. Fluid Mech.* **917**, A46.
NÉEL, B., ERININ, M. & DEIKE, L. 2022 Role of contamination in optimal droplet production by collective bubble bursting. *Geophys. Res. Lett* **49** (1), e2021GL096740.
PICO, P., KAHOUADJI, L., SHIN, S., CHERGUI, J., JURIC, D. & MATAR, O.K. 2024 Surfactant-laden bubble bursting: dynamics of capillary waves and Worthington jet at large Bond number. *Phys. Rev. Fluids* **9** (8), 083606.
PIERRE, J., POUJOL, M. & SÉON, T. 2022 Influence of surfactant concentration on drop production by bubble bursting. *Phys. Rev. Fluids* **7** (7), 073602.
POPINET, S. 2009 An accurate adaptive solver for surface-tension-driven interfacial flows. *J. Comput. Phys.* **228** (16), 5838–5866.
POPINET, S. 2018 Numerical models of surface tension. *Annu. Rev. Fluid Mech.* **50**, 49–75.
POULAIN, S., VILLERMAUX, E. & BOUROUIBA, L. 2018 Ageing and burst of surface bubbles. *J. Fluid Mech.* **851**, 636–671.
SAINI, M., SANJAY, V., SAADE, Y., LOHSE, D. & POPINET, S. 2025 Implementation of integral surface tension formulations in a volume of fluid framework and their applications to Marangoni flows. *J. Comput. Phys.* **542**, 114348.
SHAW, D.B. & DEIKE, L. 2021 Surface bubble coalescence. *J. Fluid Mech.* **915**, A105.
SHELTON, J. & TRINH, P.H. 2022 Exponential asymptotics for steady parasitic capillary ripples on steep gravity waves. *J. Fluid Mech.* **939**, A17.
STONE, H.A. 1990 A simple derivation of the time-dependent convective-diffusion equation for surfactant transport along a deforming interface. *Phys. Fluids* **2** (1), 111–112.
TAKAGI, S. & MATSUMOTO, Y. 2011 Surfactant effects on bubble motion and bubbly flows. *Annu. Rev. Fluid Mech.* **43** (1), 615–636.
TSAI, W. & LIU, K.-K. 2003 An assessment of the effect of sea surface surfactant on global atmosphere-ocean CO_2 flux. *J. Geophys. Res. Oceans* **108** (C4), 3127.
WANG, B., CHERGUI, J., SHIN, S., JURIC, D. & CONSTANTE-AMORES, C. 2025 Surfactant-laden breaking wave: regular and spilling regimes. arXiv: 2507.11876.
WANG, F., ZENG, H., DU, Y., TANG, X. & SUN, C. 2026 Marangoni-driven freezing dynamics of supercooled binary droplets. *J. Fluid Mech.* **1026**, A11.
WURL, O., WURL, E., MILLER, L., JOHNSON, K. & VAGLE, S. 2011 Formation and global distribution of sea-surface microlayers. *Biogeosciences* **8** (1), 121–135.
XU, C. & PERLIN, M. 2023 Parasitic waves and micro-breaking on highly nonlinear gravity–capillary waves in a convergent channel. *J. Fluid Mech.* **962**, A46.
XU, Y., CUI, L., JENG, D.-S., WANG, M., SUN, K. & CHEN, B. 2025 Hydrodynamic characteristics around offshore pipelines and oscillatory pore pressures in sand beds under combined random wave and current loads. *Theor. Appl. Mech. Lett.* **15** (3), 100575.
YON, S. & POZRIKIDIS, C. 1998 A finite-volume/boundary-element method for flow past interfaces in the presence of surfactants, with application to shear flow past a viscous drop. *Comput. Fluids* **27** (8), 879–902.

https://doi.org/10.1017/jfm.2026.11260 Published online by Cambridge University Press